












Vasorin as an actor of bone turnover?

Caroline Andrique¹  | Anne Laure Bonnet^{1,2}  | Julien Dang³  |
 Julie Lesieur¹  | A. Michaela Krautzberger⁴ | Brigitte Baroukh¹ |
 Coralie Torrens¹ | Jeremy Sadoine¹  | Alain Schmitt⁵ | Gael Y. Rochefort¹  |
 Claire Bardet¹  | Isabelle Six⁶  | Pascal Houillier^{7,8} | Pierre Louis Tharaux³  |
 Heinrich Schrewe⁴ | Celine Gaucher^{1,2}  | Catherine Chaussain^{1,2,9} 

¹Université Paris Cité, Montrouge, France

²AP-HP, Services de médecine bucco-dentaire: GH Nord - Université Paris Cité, GH Sorbonne Université, GH Henri Mondor, Paris, France

³Paris Cardiovascular Research Centre – PARCC, Université Paris Cité, Inserm, Paris, France

⁴Department of Developmental Genetics, Max Planck Institute for Molecular Genetics, Berlin, Germany

⁵Université Paris Cité, Institut Cochin, INSERM U1016, CNRS UMR8104, Paris, France

⁶URP 7517 UPJV, Pathophysiological Mechanisms and Consequences of Cardiovascular Calcifications (MP3CV), Jules Verne University of Picardie, Amiens, France

⁷Centre de Recherche des Cordeliers, INSERM U1138, Sorbonne Université, Université Paris Cité, Paris, France

⁸AP-HP, Explorations fonctionnelles rénales, Physiologie, Hôpital européen Georges-Pompidou, Paris, France

⁹APHP, Centre de référence des maladies rares du phosphate et du calcium (filière OSCAR, ERN BOND), Hôpital Bretonneau, Paris, France

Correspondence

Catherine Chaussain, Université Paris Cité,
URP 2496, 1 rue Maurice Arnoux, F-92120
Montrouge, France.
Email: catherine.chaussain@u-paris.fr

Funding information

Agence Nationale de la Recherche,
Grant/Award Number: 17-CE14-0028;
Fondation pour la Recherche Médicale,
Grant/Award Number: DGE2011123012

Abstract

Bone diseases are increasing with aging populations and it is important to identify clues to develop innovative treatments. *Vasn*, which encodes vasorin (Vasn), a transmembrane protein involved in the pathophysiology of several organs, is expressed during the development in intramembranous and endochondral ossification zones. Here, we studied the impact of *Vasn* deletion on the osteoblast and osteoclast dialog through a cell Coculture model. In addition, we explored the bone phenotype of *Vasn* KO mice, either constitutive or tamoxifen-inducible, or with an osteoclast-specific deletion. First, we show that both osteoblasts and osteoclasts express *Vasn*. Second, we report that, in both KO mouse models but not in osteoclast-targeted KO mice, *Vasn* deficiency was associated with an osteopenic bone phenotype, due to an imbalance in favor of osteoclastic resorption. Finally, through the Coculture experiments, we identify a dysregulation of the Wnt/ β -catenin pathway together with an increase in RANKL release by osteoblasts, which led to an enhanced osteoclast activity. This study unravels a direct role of *Vasn* in bone turnover, introducing a new biomarker or potential therapeutic target for bone pathologies.

C. Andrique and A. L. Bonnet are co-first authors.

H. Schrewe, C. Gaucher, and C. Chaussain are co-senior authors.

This is an open access article under the terms of the [Creative Commons Attribution-NonCommercial-NoDerivs](https://creativecommons.org/licenses/by-nc-nd/4.0/) License, which permits use and distribution in any medium, provided the original work is properly cited, the use is non-commercial and no modifications or adaptations are made.

© 2024 The Authors. *Journal of Cellular Physiology* published by Wiley Periodicals LLC.

KEYWORDS

bone, osteoblast, osteoclast, physiology

1 | INTRODUCTION

Vasorin (Vasn), a cell surface protein encoded by *Vasn* (aka *Slit-like 2*), was identified in several vertebrates including zebrafish, rodents and humans (Bonnet et al., 2018; Ikeda et al., 2004). Vasn is highly conserved at the DNA and protein levels, suggesting a highly conserved function throughout evolution (L. Chen et al., 2005). The use of a *Vasn^{lacZ}* knock-in reporter mouse strain indicated that Vasn was expressed at various stages of embryonic and fetal development in the media of large vessels and in various developing organs. In particular, a positive signal was seen in the skeletal system, starting as early as the first mesenchymal condensations and at embryonic day 17.5, in the ossification regions of the long bones (Krautzberger et al., 2012).

In adult mice, Vasn is expressed in several organs, such as the kidney and liver. In the liver, Vasn is involved in glycogen metabolism upstream of hepatocyte autophagy, as its deletion upregulates hepatocyte autophagy through the mTOR-ULK1 signaling pathway (Yang et al., 2022). Vasn regulation is important during vessel repair as shown in a rat arterial injury model (Ikeda et al., 2004). Accordingly, we reported the role of Vasn in vascular smooth muscle cells (VSMC) for vascular function maintenance (Louvet et al., 2022).

In humans, Vasn was identified in several pathological tissues such as cancer tissues (Liang et al., 2023; Liu et al., 2021; Man et al., 2018; Yu-Lee et al., 2019). Vasn was recovered in the plasma and urine of patients with nephropathies and acute rejection of renal transplant, and was then proposed as a biomarker of these disorders (Ahn et al., 2010; Loftheim et al., 2012; Moon et al., 2011; Samavat et al., 2015). Vasn was also detected in the synovial fluid of patients with osteoarthritis, unraveling a potential role for this protein in osteo-articular pathologies (Balakrishnan et al., 2014).

In vascular smooth muscle cells (VSMC), Vasn plays a role in the TGF- β pathway (Ikeda et al., 2004), a critical pathway for bone development and remodeling (Guasto & Cormier-Daire, 2021); however, to date, there is no evidence for a role of Vasn in bone or other mineralized tissues pathophysiology. Vasn overexpression was reported to promote tumor progression by activating either the YAP/TAZ (Liang et al., 2023; Liu et al., 2021) or the Notch/STAT3 signaling pathways (Liang et al., 2019). In the latter, Vasn overexpression was reportedly driven by hypoxia, primarily through the expression of HIF-1 α (Man et al., 2018). The Notch signaling pathway is important in bone pathobiology for its roles in the remodeling and regenerative processes, although with antagonist effect during development and remodeling (Guasto & Cormier-Daire, 2021). Studies demonstrated a direct role of the YAP/TAZ signaling pathway in some bone pathologies, such as Ewing's sarcoma and osteosarcomas (Kovar et al., 2020), and this pathway has a critical role in regulating the WNT signaling pathway under mechanical loading (Kovar et al., 2020).

As Vasn i) is expressed in the ossification regions of long bones during development and ii) is involved in signaling pathways that are essential for bone metabolism, we hypothesized that Vasn may intervene in bone physiology, and its dysregulation may be associated with bone disorders. In this study, we used constitutive (*Vasn^{null}*) and conditional (*Vasn^{fllox}*) *Vasn* knock-out mice to investigate the role of Vasn in bone pathophysiology. We show that Vasn is expressed in both osteoblasts and osteoclasts and that its expression regulates the osteoblast-osteoclast dialog through several signaling pathways, including the Wnt/ β -catenin pathway, and increased RANKL release.

2 | RESULTS

2.1 | Skeleton phenotype of *Vasn*-deficient mice

Constitutive *Vasn* KO mice, which die between postnatal Day 21 (D21) and D24 (Bonnet et al., 2018), exhibit a growth failure from post-natal D14 to D21 when compared with their wild type (WT) littermates (Figure 1a) as shown by micro-CT (μ CT) measurements of the whole body and of the femur at D21. Their axial skeletal size was reduced versus (vs) WT mice ($p = 0.0339$) (Figure 1b). Also, the microarchitecture of the distal femoral metaphysis was altered: the bone volume/total volume (BV/TV) versus WT ones (2.83% vs. 5.27%, $p = 0.0043$), the trabeculae number (0.472 vs. 0.811, $p = 0.0006$) and thickness (0.060 vs. 0.066 mm, $p = 0.012$) were significantly decreased (Figure 1c). In contrast, the cortical area fraction (Ct. Ar/Tt. Ar) and the cortical thickness (Ct. Th) were similar in WT and KO mice (Supporting Information S1: Figure S1A). Histologically, there was no difference in the growth plate of the femur distal metaphysis between constitutive *Vasn* KO and WT mice. Cell proliferation (PCNA immunohistochemistry), together with the height of proliferative and hypertrophic zones were undisturbed, indicating maintenance of the growth plate (Supporting Information S1: Figure 1B). Of note, at D21, we found no difference for these bone parameters, except for trabecular separation, between *Vasn* heterozygous mice and their WT littermates (Supporting Information S1: Figure S2). Blood analysis showed no difference in plasma -calcium and -phosphate concentrations in *Vasn* KO mice compared to WT mice, whereas there was a significant decrease in the active vitamin D in *Vasn* KO blood compared to WT (Figure 1d). For all the experiments reported in this model, no sex difference was observed.

2.2 | Osteoclast and osteoblast activities in *Vasn*-deficient mice

As *Vasn* KO displayed highly disturbed bone microarchitecture, we investigated osteoclastic activity in *Vasn* KO and WT littermates.

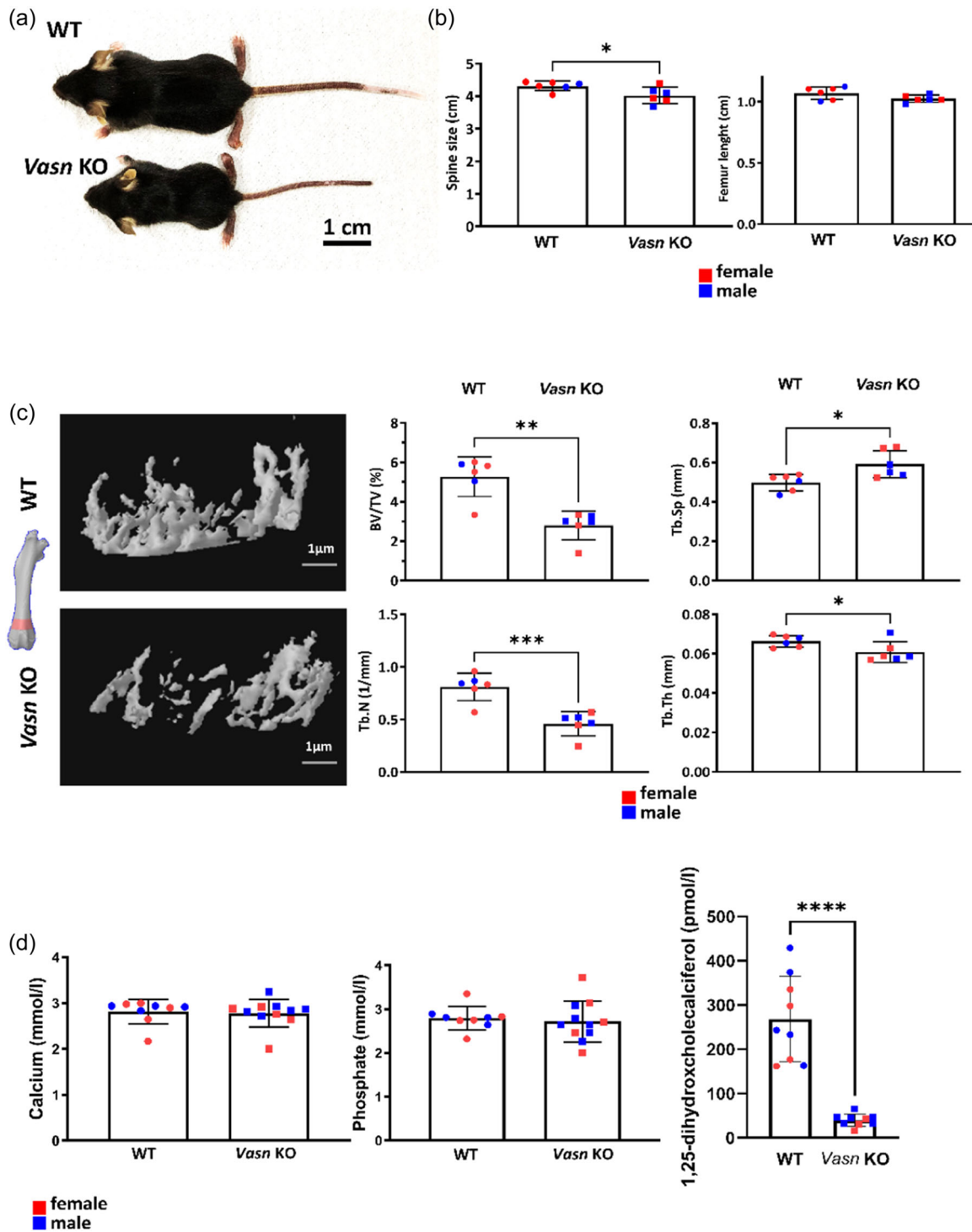


FIGURE 1 Skeleton phenotype of constitutive *Vasn* KO mice. Constitutive *Vasn* KO mice skeleton was studied at post-natal day 21 ($n = 6$ per group, males are represented in blue, females are represented in red). (a) General body views showing that *Vasn* KO mice are smaller than their WT littermates. (b) In vivo μ CT analysis of the skeleton showed significantly reduced spine size in *Vasn* KO mice compared to WT and no difference in the femur length. Results are expressed as mean \pm SD. * represents a significant difference $p < 0.05$ (c) Visualization by 3D reconstruction of the femur trabeculae and μ CT analysis of bone microarchitecture parameters (BV/TV, Tb.N and Tb.Th and Tb.Sp). Results are expressed as mean \pm SD. * represents a significant difference $p < 0.05$, ** $p < 0.01$, *** $p < 0.001$. (d) Blood serum analysis of calcium, phosphate, and 1,25-dihydroxycholecalciferol. **** indicates $p < 0.0001$.

Osteoclasts were revealed by Tartrate-Resistant Acid Phosphatase enzymatic reaction (TRAP) at the level of the secondary *spongiosa*. The resorption area (TRAP-positive area/total trabeculae area) was almost two times higher in *Vasn* KO mice compared with WT (28% vs. 16%; $p = 0.0286$) (Figure 2a). At the TEM level, osteoclast ultrastructure appeared to be similar in the constitutive KO and WT groups, with a well-distinguishable ruffled border that covered a large bone surface (Figure 2b).

The osteoblastic activity assessed by serum alkaline phosphatase (ALP) was not modified in the *Vasn* KO group compared to WT mice (456.9 vs. 564.1 U/L) (Figure 2a). Consistent with serum ALP, osteoblast ultrastructure appeared to be similar in both groups, with a well-developed endoplasmic reticulum, indicating intense matrix secretory activity (Supporting Information S1: Figure S3). Osteocyte ultrastructure was not altered in *Vasn* KO long bones as well. (Figure 2b, right lower insight; Supporting Information S1: Figure S3).

2.3 | Skeleton phenotype of adult inducible-*Vasn* KO mice

We then investigated whether the deletion of *Vasn* in adult mice was also associated with an altered bone phenotype. For all the experiments reported in this model, no sex difference was observed. Eight-week-old inducible *Vasn* KO mice (*Vasn*^{*fllox/fllox*}; CAGGCre-ERTM) were treated with intraperitoneal injections of tamoxifen or vehicle (peanut oil) for 5 days. At day 22 (D22) postinjection, we studied the microarchitecture of the distal femoral metaphysis using μ CT acquisitions in these mice (Figure 3). The BV/TV was significantly lower in the tamoxifen-induced *Vasn* KO group when compared with their vehicle only controls (7.1% vs. 13.6%, $p = 0.011$), their trabeculae were less numerous (Tb.N: $p = 0.024$) (Figure 3a). In contrast, similar to constitutive *Vasn* KO mice, the mid-diaphysis cortical area fraction and thickness were not modified (Fig. S4). Serum analysis showed hypercalcemia in tamoxifen-induced *Vasn* KO mice compared with the vehicle group, whereas plasma phosphate concentration was similar in both groups (Figure 3b).

At D22, osteoclast activity was enhanced in tamoxifen-induced *Vasn* KO mice, indeed the resorption area (Oc. S/BS) was significantly increased when compared with the vehicle-treated group (32% vs. 23%; $p = 0.009$). In contrast, the osteoblast activity did not seem to be different between the groups (Figure 4a); accordingly, serum ALP was similar in both groups (Figure 4a). However, double calcein/demeclocycline labeling showed increased mineral apposition rate in tamoxifen-induced *Vasn* KO mice compared to vehicle-treated group (Figure 4b). The ultrastructure of osteoclasts was similar in tamoxifen and control *Vasn* KO groups (Figure 4c). The same observation was made for osteoblasts, which exhibited a rich network of endoplasmic reticulum, and for osteocytes (Supporting Information S1: Figure S5).

2.4 | Skeleton phenotype of osteoclast-specific *Vasn* KO mice

As increased osteoclast activity was observed in both *Vasn*-deficient mouse models, we generated osteoclast-specific inducible *Vasn* KO mice by expressing Cre-recombinase under the control of the cathepsin K promoter (Sanchez-Fernandez et al., 2012). Three-month-old inducible Ctsk-Cre *Vasn* KO mice received repeated tamoxifen or vehicle injection. At 3 weeks after induction, no difference in terms of femur microarchitecture (trabecular and cortical parameters) was observed between tamoxifen or vehicle-induced mice (Supporting Information S1: Figure S6A and S7). Furthermore, the osteoclast activity (Oc. S/BS) remained unchanged (Supporting Information S1: Figure S6B). For all the experiments reported in this model, no sex difference was observed.

2.5 | In vitro functional assays with *Vasn* KO osteoclasts

As, in our hands, no reliable antibody was available to obtain a specific signal for *Vasn* by immunohistochemistry in mouse tissues, *Vasn* expression was investigated in primary cells by Western blot. Monocytes were isolated from the bone marrow of constitutive *Vasn* KO and WT littermates and differentiated into osteoclasts in specific culture medium. At D7, Western blot analysis of the WT cell lysates revealed a band at 110 kDa, whereas no signal was found in *Vasn* KO lysates, supporting that osteoclasts actually expressed *Vasn* (Figure 5a).

We next aimed to understand the origin of the bone loss observed in constitutive *Vasn* KO murine models. We first hypothesized that this loss may be a consequence of an increased number of osteoclasts, so we cultured bone marrow-derived monocytes on plastic plates. Seven days after differentiation with RANKL and M-CSF, TRAP-positive cells were counted and classified into four groups according to their cell diameter, reflecting the osteoclast differentiation stage (Tsukasaki & Takayanagi, 2022). No significant changes were observed between *Vasn* KO cells and their WT counterparts in the four groups (Figure 5b). Then, to test whether osteoclast activity was modified, WT and *Vasn* KO osteoclasts were cultured on bone slices, which constitute a more physiological environment than plastic (Kleinhans et al., 2015). Quantification of the total resorption area at D10 showed no significant difference between *Vasn* KO and WT cells. The depth of resorption pits was measured by reflection on a confocal microscope and no significant difference was found (Figure 5c). Taken together, these data showed that in vitro osteoclast activity was unaffected by *Vasn* deletion. However, as *Vasn* KO mice displayed an increased osteoclast activity compared to WT, we performed RNA sequencing analysis in osteoclasts cultured on resorption plates. Functional analysis using the Gene set enrichment (GSEA) showed significant changes of several signaling pathways in *Vasn* KO osteoclasts compared to WT (20 in total; Supporting

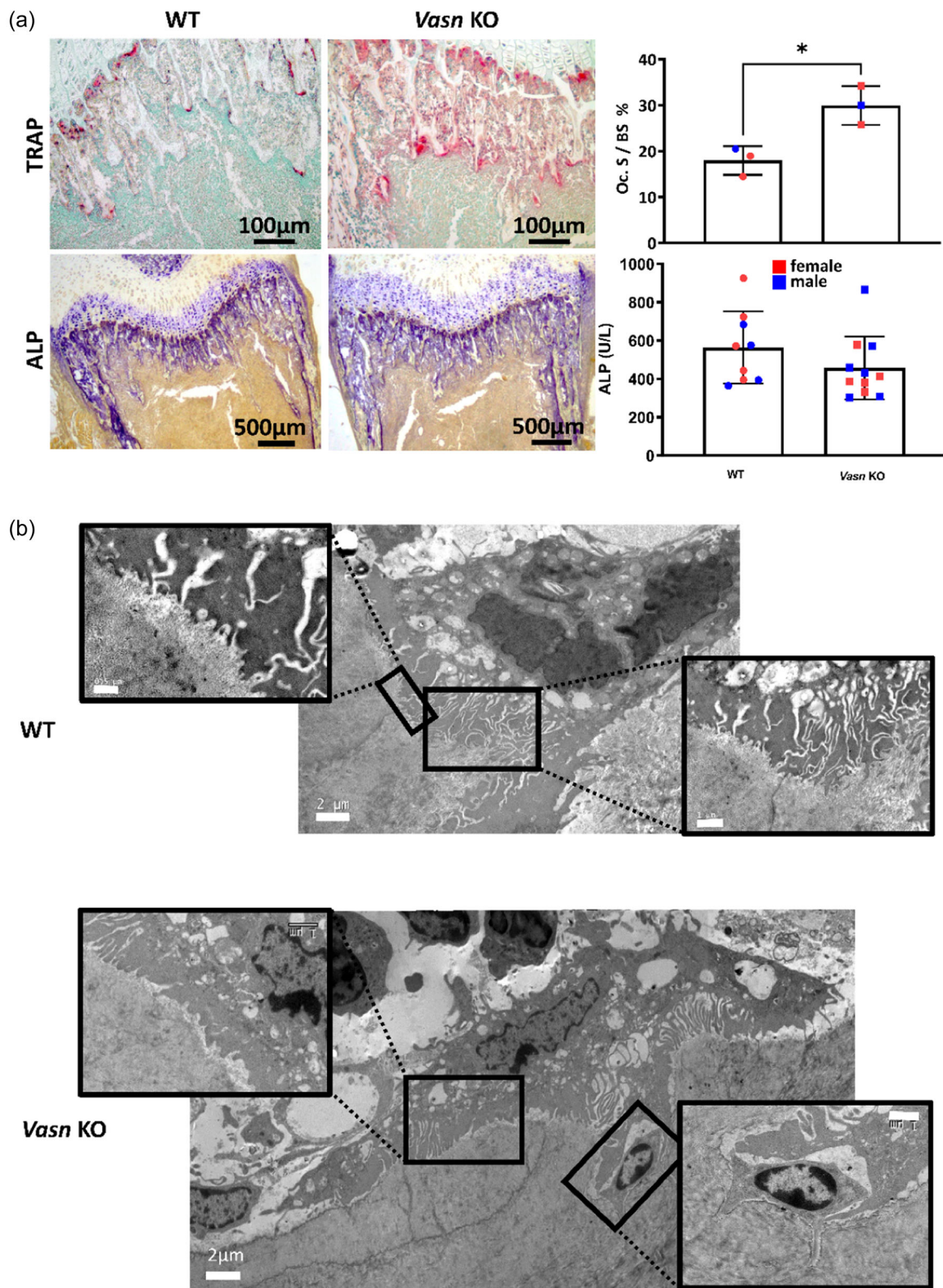


FIGURE 2 Bone cell phenotype of constitutive *Vasn* KO mice. (a) TRAP and ALP staining were performed on methyl methacrylate sections of *Vasn* KO and WT femurs at postnatal Day 21 (D21), TRAP-positive osteoclast surface/Bone total Surface (OC S/BS) was quantified with ImageJ software ($n = 4$, males are represented in blue, females are represented in red). ALP was quantified in the blood serum of *Vasn* KO and WT mice ($n = 9$ mice per group, males are represented in blue, females are represented in red). Results are expressed as mean \pm SD. * represents a significant difference ($*p < 0.05$). (b) TEM analysis of OC ultrastructure in *Vasn* KO and WT mice. The ruffled border and sealing zone are well-distinguishable (insights). The osteocyte ultrastructure is not altered in *Vasn* KO mice; the osteocyte is surrounded by an osteoclast ruffled border (right lower insight).

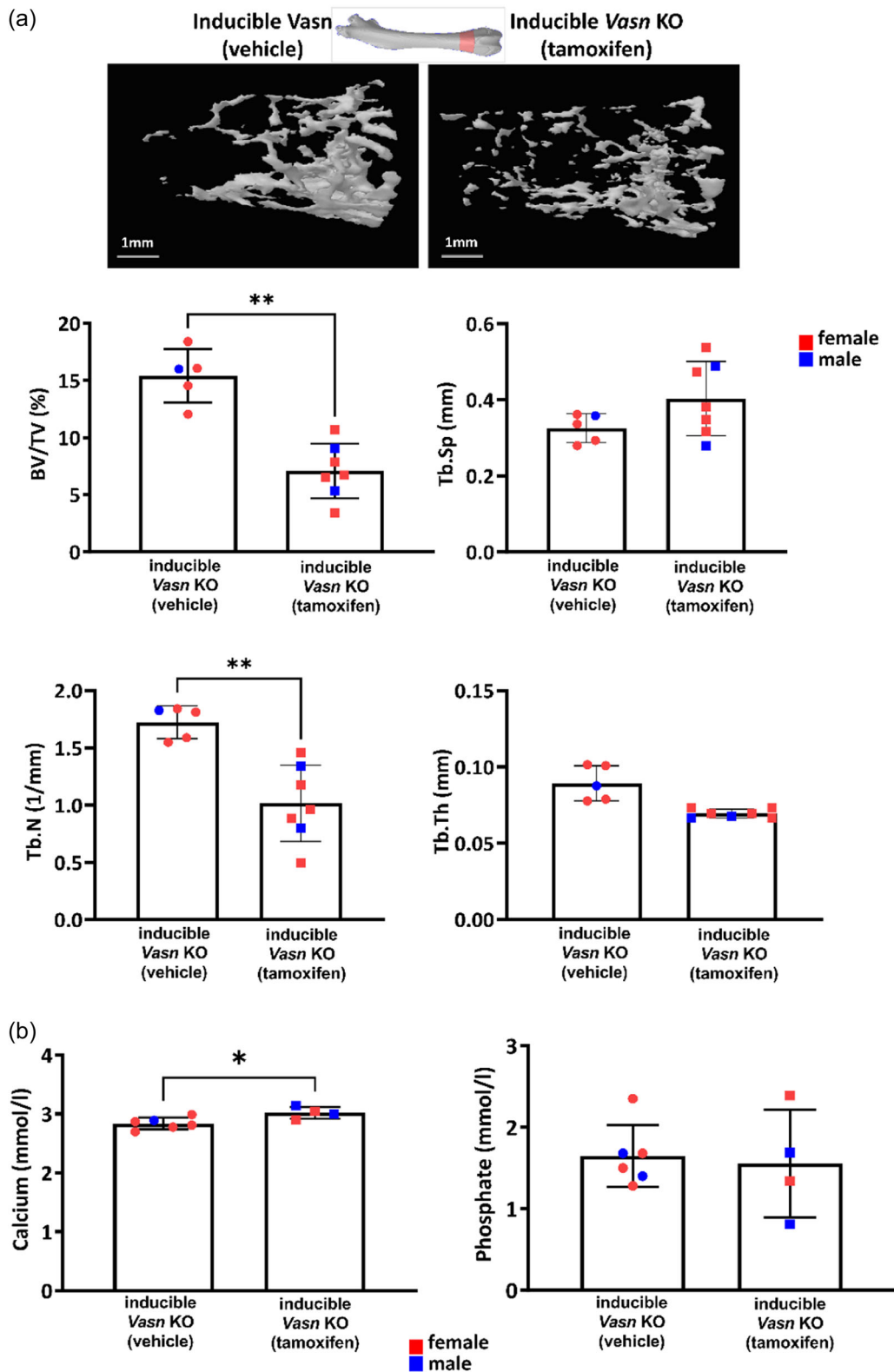


FIGURE 3 Skeleton phenotype of adult inducible *Vasn* KO mice. (a) At Day 22 (D22) after tamoxifen or vehicle injection, visualization by 3D reconstruction of the femur trabeculae and μ CT analysis of bone microarchitecture parameters (BV/TV, Tb.N and Tb. Th and Tb. Sp). (b) Blood analysis of calcium and phosphate in tamoxifen-induced *Vasn* KO mice compared to vehicle-induced ones ($n = 6$ mice per group). Results are expressed as mean \pm SD. * represents a significant difference $**p < 0.01$. Males are represented in blue, females are represented in red.

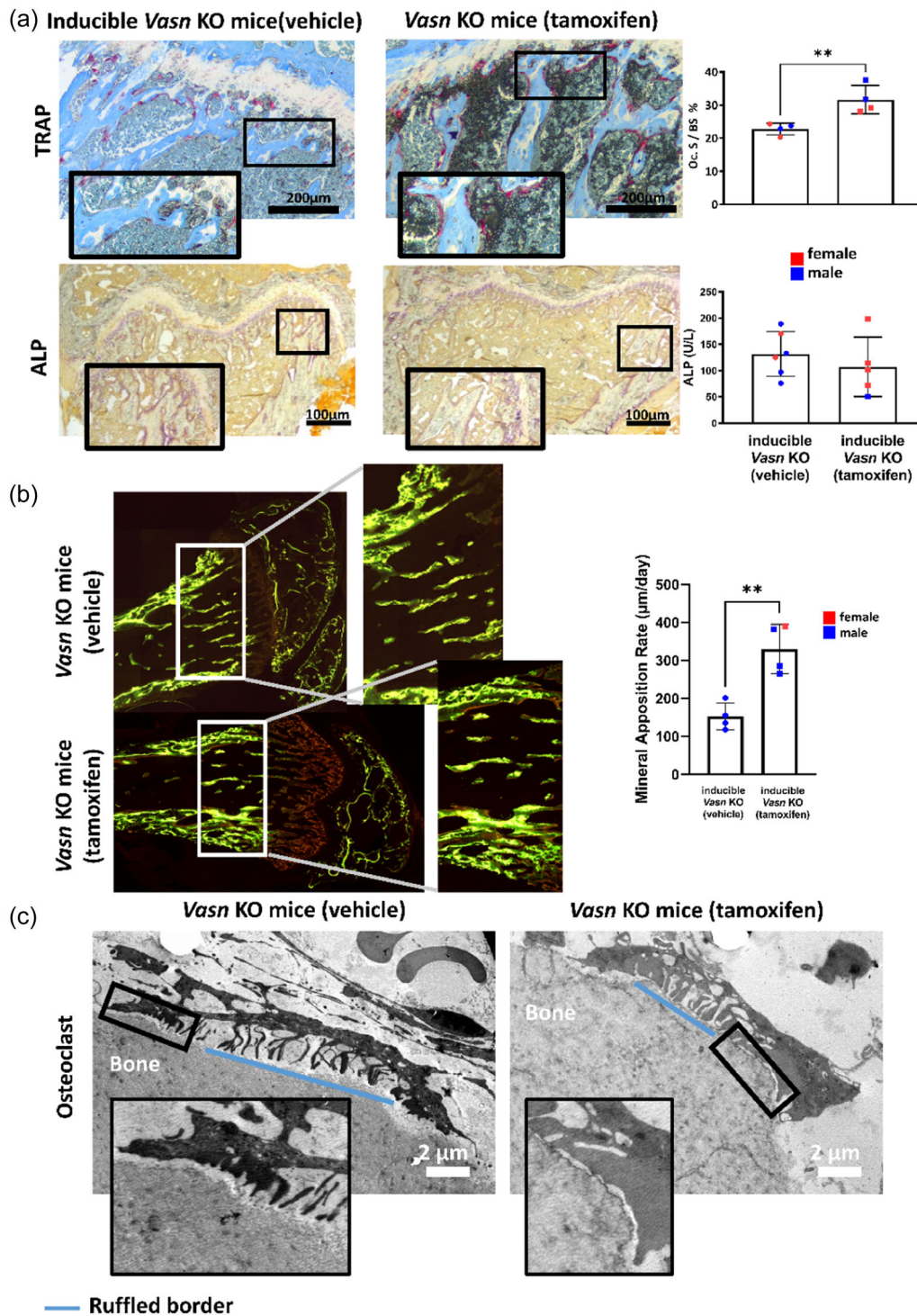


FIGURE 4 Bone cell phenotype of adult inducible *Vasn* KO mice. (a) TRAP and ALP staining were performed on methyl methacrylate sections of tamoxifen- and vehicle-induced *Vasn* KO femurs. TRAP-positive osteoclast surface/Bone total Surface (OC S/BS) was quantified with ImageJ software ($n = 4$ mice per group, males are represented in blue, females are represented in red). ALP was measured in the blood serum in both groups ($n = 6$ mice per group, males are represented in blue, females are represented in red). Results are expressed as mean \pm SD. * represents a significant difference $*p < 0.05$. (b) Mineral apposition rate (MAR) measured in the trabeculae (insight) at the secondary spongiosa level of femurs ($n = 4$ mice per group, males are represented in blue, females are represented in red). Results are expressed as mean \pm SD. * represents a significant difference $**p < 0.01$. (c) TEM analysis of osteoclast (OC) ultrastructure in tamoxifen and vehicle-induced *Vasn* KO mice. The ruffled border (blue line) and sealing zone (insights) are well distinguishable.

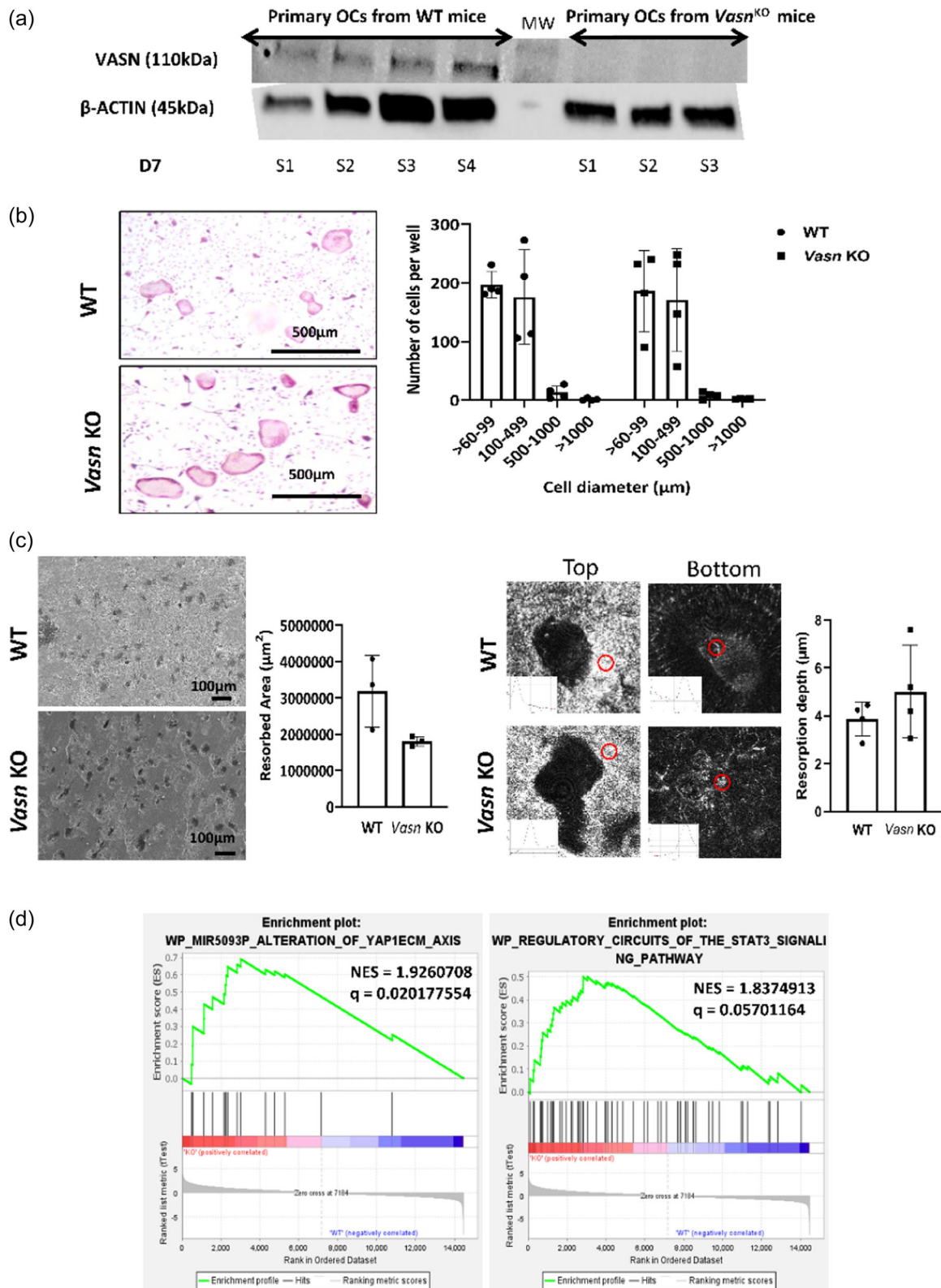


FIGURE 5 (See caption on next page).

Information S1: Table S2), particularly an enrichment in the WikiPathway database of YAP1-ECM axis and in the WikiPathway database of regulatory circuits of STAT3 (Figure 5d). Both pathways are known to be important for the osteoclast resorbing activity (Hou & Tian, 2022; Yang et al., 2018).

2.6 | In vitro functional assays of *Vasn* KO osteoblasts

Vasn KO and WT osteoblast progenitors derived from the calvaria were induced toward osteogenic differentiation for 7, 14 and 21 days. At D7, Western blot analysis of the cell lysates revealed a weak band at 110 kDa, which gradually increased up to D21, indicating that *Vasn* is expressed by WT osteoblasts and that its expression is enhanced during the differentiation process. (Figure 6a) At D7, 14, and 21, mineralization was assessed by alizarin red staining and osteoblast activity by ALP assay (Figure 6b). At all-time points, ALP activity was strong and similar in WT and KO osteoblasts. Alizarin red staining gradually increased from D7 to D21 in both groups; at D21, the staining appeared stronger in *Vasn* KO cultures. Quantification of alizarin red absorbance showed that there was a significant increase in matrix mineralization in *Vasn* KO cultures at this time point (Figure 6b).

We next measured the release of cytokines in osteoblast culture supernatants using a luminex immunoassay. We focused on cytokines that could be involved in bone cell cross-talk such as RANKL, M-CSF, VEGF, IL-6, osteopontin and IL-1 β (Supporting Information S1: Figure S8). At D14 and D21, we measured a significant increase in RANKL (Figure 6c), an activator of osteoclastogenesis (Boyce & Xing, 2008), in the *Vasn* KO osteoblast supernatants compared to the WT ones.

Finally, we performed RNA sequencing analysis on osteoblasts at D14 of the differentiation process. GSEA showed significant modification of several pathways in *Vasn* KO osteoblasts compared to WT cells (35 in total; Supporting Information S1: Table S3), including an enrichment in REACTOME database of pre-Notch expression and processing, and in REACTOME database of the formation of the β -catenin complex (Figure 6d). Both pathways are important for osteoblast activity (Baron & Kneissel, 2013; Canalis et al., 2013).

2.7 | Co-cultures of *Vasn* KO osteoblasts and osteoclasts

Co-cultures were conducted to investigate whether the dialog between osteoblasts and osteoclasts was altered by the absence of *Vasn* (Figure 7a). As RANKL release was increased in the primary culture of *Vasn* KO osteoblasts (Figure 6c), we used a transwell culture system that allows the passage of soluble cytokines but not direct contact between the two cell types (Mansouri et al., 2015). RT-qPCR analyses were performed after 10 days of Coculture (Figure 7b and Figure 8). Consistent with the RNA-seq analysis (Figure 6e), *Vasn* KO osteoblasts cocultured with *Vasn* KO osteoclasts showed an inhibition of the Notch pathway, evidenced by a decreased expression of two target genes of this pathway (*Hes1* and *Heyl*) (Ballhause et al., 2021) (Figure 7b). In addition, we found an activation of the Wnt/ β -catenin pathway, evidenced by an increased expression of two target genes (*Tcf1* and *Lef1*) (Baron & Kneissel, 2013). This was confirmed at the protein level by Western blot analysis showing significantly higher activation of β -catenin in the double KO group (OB *Vasn* KO/Oc *Vasn* KO) compared with the other groups ($p < 0.05$) (Figure 7c). Furthermore, the expression of genes related to osteoblast activity, namely *Runx2*, *Alpl* and *Col2A1* (Ponzetti & Rucci, 2021), was significantly enhanced in KO osteoblasts compared to WT ones. Of note, this increase was stronger when the cocultured osteoclasts were KO. Whatever was the origin of the cocultured osteoclasts (WT or KO), there was a significant increase in the expression of *Tnfsf11*, which encodes RANKL (Chambers, 2000).

Vasn KO osteoclasts cocultured with *Vasn* KO osteoblasts exhibited a significant increase in *Stat3* (Chen et al., 2020; Cheng et al., 2017; Xue et al., 2022), and in genes related to the YAP/TAZ pathway (*Tead4*, *Yap1* and *Taz*) (W. Yang et al., 2018; Zhao et al., 2018), which is consistent with our RNA-seq analysis (Figure 5d). We also found a significant increase in genes related to osteoclast late differentiation (*integrin* β 3), bone resorption including mineral dissolution (*Tcirg1*, *Cln7*, *Car2*, which encode H⁺-ATPase subunits) and matrix degradation (*Acp5*, *Ctsk* and *MMP9*) (Boyle et al., 2003) (Figure 8a). Western blot analysis revealed that the STAT3 pathway was activated in all the Coculture groups, evidenced by a significant increase in STAT3 phosphorylation. However, the pSTAT3/STAT3 ratio was higher whenever, at least, one of the cell type was *Vasn* KO (Figure 8b). TRAP staining of co-cultures showed

FIGURE 5 In vitro functional assays with *Vasn* KO osteoclasts. (a) Western blot analysis of *Vasn* KO and WT osteoclast lysates performed with a vasorin antibody. Four different samples were studied from four different mice (S1–S4). A positive signal was observed at 110 kDa in WT lysates that was completely absent in KO ones (b) Bone marrow-derived *Vasn* KO and WT monocytes were cultured on plastic under osteoclastic conditions for 7 days. At D7, TRAP staining (in pink) and cell counting showed no difference between *Vasn* KO and WT samples. For counting, cells were divided into four groups according to their diameter. (c) Bone marrow-derived monocytes were cultured on bone slices under osteoclastic conditions for 10 days. At Day 10 (D10), SEM acquisitions were performed and quantification of the total resorption area was calculated. To measure the depth of resorption pits, two measures of the z-axis profile were performed: one at the top of bone surface, the second at the bottom of the resorption pit. The depth of each pit was obtained by calculating the delta between these two points. No differences were found between the groups. Results are expressed as mean \pm SD. (d) RNA sequencing was performed on bone marrow-derived monocytes cultured on bone slices under osteoclastic conditions for 10 days. NES is normalized enrichment score. Results are expressed in q -value < 0.05 .

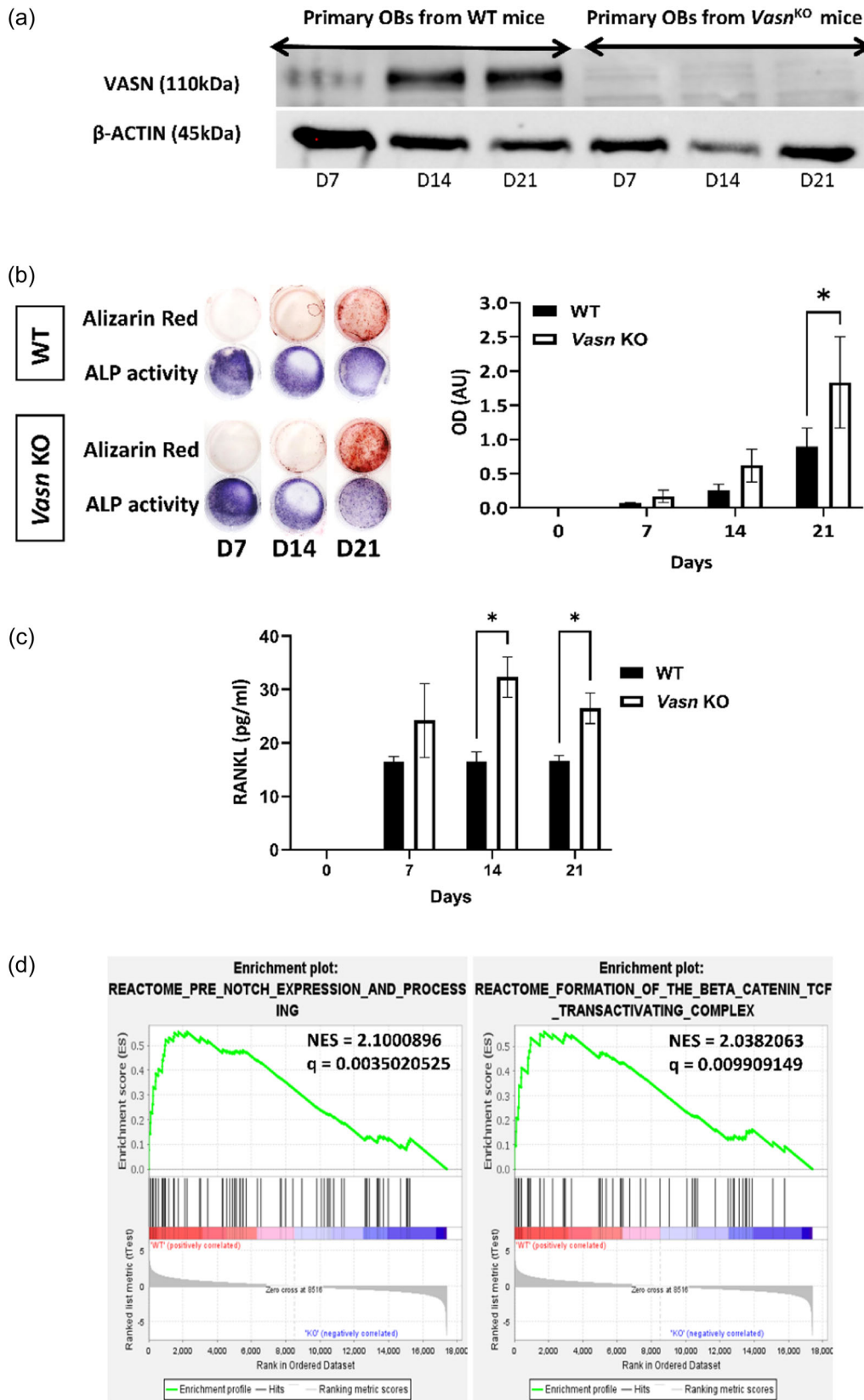


FIGURE 6 (See caption on next page).

large osteoclasts with robust TRAP activity in double *Vasn* KO co-cultures compared to WT co-cultures (Figure 8c).

We finally went back to the constitutive *Vasn* KO mouse model to validate the Coculture findings. RNA-scope using *Runx2* and *CtsK* fluorescent probes revealed that there was a simultaneous increase in *Runx2* (bone formation) and *CtsK* (bone resorption) RNA expression in bone cells residing on the trabeculae in *Vasn* KO mice compared to WT, confirming that *Vasn* depletion enhanced bone turnover (Figure 9a). Taken together, our data unravel an altered dialog between osteoblasts and osteoclasts when *Vasn* is absent, with an imbalance in favor of osteoclast activity (Figure 9b).

3 | DISCUSSION

Vasn, a transmembrane protein involved in the pathophysiology of several organs including the large vessels and the kidney (Ikeda et al., 2004; Louvet et al., 2022; Man et al., 2018), is also expressed in the skeleton during development (Krautzberger et al., 2012). In the present study, we investigated the role of *Vasn* on long-bone pathophysiology. First, we report that the absence of *Vasn* resulted in abnormal bone phenotype, which progressively settled after birth in constitutive *Vasn* KO animals or a couple of weeks after *Vasn* deletion in adult mice. Of note, we did not observe a difference between male and female mice in any of the models, suggesting that the role of *Vasn* is independent of the sex of the animal. Second, we show that *Vasn* is expressed in both osteoblasts and osteoclasts, the main cells responsible for bone remodeling (Raggatt & Partridge, 2010). We also unravel *Vasn* involvement in several and distinct signaling pathways that are important for the osteoblast-osteoclast dialog as well as an important release of soluble RANKL by KO osteoblasts. Thus, the osteopenic bone phenotype observed in these models resulted from an unbalanced bone turnover in favor of osteoclast activity.

In vitro culture of osteoblast progenitors under mineralizing conditions revealed that the absence of *Vasn* was associated with higher mineral deposition in the cultures. These data were corroborated by double calcein/demeclocycline labeling showing increased mineral apposition rate in adult *Vasn* KO mice. Interestingly, higher mineralization was previously reported in cultures of *Sost* KO osteoblast progenitors (Koide et al., 2022) or when sclerostin was inhibited in the culture media by a specific antibody (Tanaka & Matsumoto, 2021), as sclerostin is a negative regulator of the Wnt- β -catenin signaling pathway. Here, both our RNA-seq and qPCR

analyses indicated that the Wnt- β -catenin signaling pathway was upregulated in *Vasn* KO osteoblasts, which is consistent with the higher amount of mineral apposition found in the cultures. Furthermore, this pathway was activated both at RNA and protein levels in *Vasn* KO osteoblasts cocultured with *Vasn* KO osteoclasts. To the best of our knowledge, this is the first time that *Vasn* is associated to the Wnt- β -catenin signaling pathway.

TGF- β pathway was initially associated to *Vasn* in large vessel pathophysiology; *Vasn* was directly able to bind to TGF- β to modulate the cellular response during vessel repair (Ikeda et al., 2004). As this pathway is important for bone formation (Jann et al., 2020), it was tempting to hypothesize that *Vasn* deletion might alter this pathway in bone metabolism. However, our Coculture data did not support this hypothesis, as the TGF- β pathway was unchanged in *Vasn* KO osteoblasts whatever the condition was (Figure 7b). In contrast, we found that the Notch pathway was downregulated in *Vasn* KO osteoblasts. This pathway was previously shown to be hyper-activated in glial cells by hypoxic conditions in the tumor, which induced *Vasn* overexpression (Man et al., 2018). *Vasn* was shown to act as a competitive inhibitor of Numb known to reduce Notch turnover, thus increasing Notch signaling under hypoxic stress. Accordingly, here, in the absence of *Vasn*, Notch was downregulated in bone cells, evidenced by the lower expression of *Hes1* and *HeyL*, two target genes of this pathway (Kopan, 2012). These data are consistent with a recent study showing that the injection of *Vasn*-containing small extracellular vesicles in the intervertebral disc resulted in a *Vasn*-Notch1 interaction activating the Notch-signaling pathway leading to the proliferation, migration and anabolism of *nucleus pulposus* cells, delaying intervertebral disc degeneration (Liao et al., 2022).

Interestingly, both *Hes1* and *HeyL* encode inhibitors of the Wnt/ β -catenin pathway (Pakvasa et al., 2021), which limit osteoblast differentiation by inhibiting *Runx2* expression and the Tcf/Lef complex (Lin & Hankenson, 2011; Pakvasa et al., 2021). Canalis et al. reported that the effect of Notch1 on osteoblastic cells was dependent on their differentiation stage (Zanotti & Canalis, 2013). Hence, Notch1 overexpression in osteoblastic precursors led to increased bone mass (Engin et al., 2008), whereas, in mature osteoblasts, it was rather associated with lower bone volume and trabecular structure (Zanotti et al., 2008). As *Notch1* KO embryos die during early development (Swiatek et al., 1994), mice with an osteoclast-specific *Notch1*-deficiency were developed, they show a high osteoclast activity evidenced by increased osteoclast surface/bone surface and eroded bone surface (Zanotti et al., 2008), which is

FIGURE 6 *In vitro* functional assays with *Vasn* KO osteoblasts. (a) *Vasn* KO and WT osteoblasts progenitors were cultivated under osteogenic conditions for 7, 14 and 21 days before total protein extraction. In WT lysates, a band was observed at 110 kDa, which gradually increased during the osteoblast differentiation process. No signal was observed in *Vasn* KO samples. (b) Alizarin Red staining and ALP activity were performed at D7, D14 et D21. Alizarin Red quantification was made by spectrophotometry ($n = 3$) Results are expressed as mean \pm SD. * represents a significant difference ($*p < 0.05$). (c) Supernatants were collected at each time point (D7, D14 et D21) and a multiplex immunoassay measured RANKL release. Results are expressed as mean \pm SD. * represents a significant difference ($*p < 0.05$). (d) RNA sequencing was performed at D14 of osteogenic differentiation. NES is normalized enrichment score. Results are expressed in q -value < 0.05 .

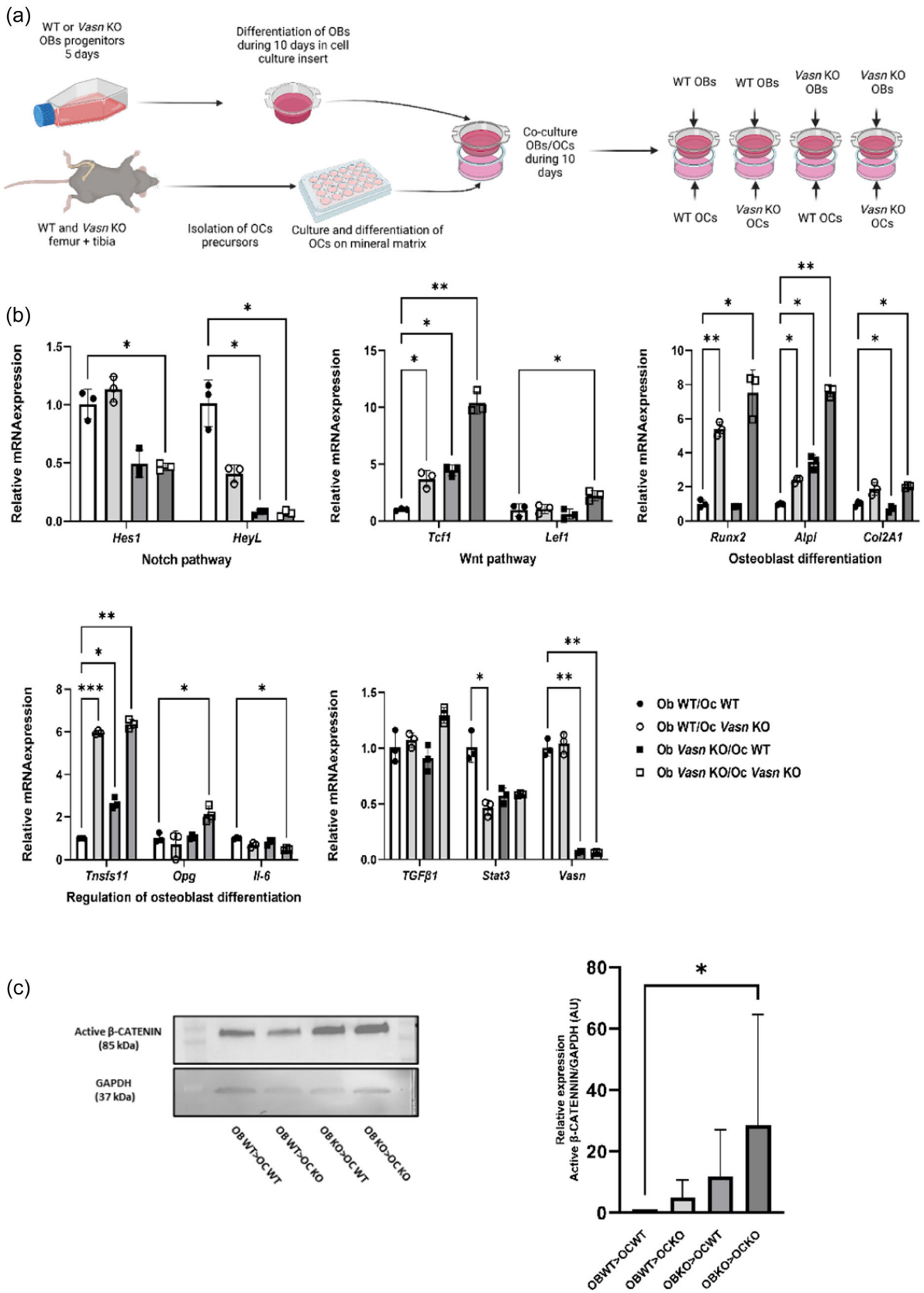


FIGURE 7 (See caption on next page.)

consistent with our findings in complete *Vasn* KO mouse models. Furthermore, as shown by our Western blot analysis, *Vasn* was enhanced during osteoblast differentiation. It appears relevant in the future to investigate whether *Vasn* is a direct regulator of the Wnt/ β -catenin pathway or an indirect one through the Notch pathway.

Murine models with an alteration of a gene related to osteoclast function display altered bone phenotypes (Udagawa et al., 2021). For example, Boskey et al. reported that the ablation of Cathepsin K activity led to hypermineralization of the long bones. (Boskey et al., 2009). On the contrary, *Sirt6* null mice experiencing excessive osteoclast activation exhibited osteopenia (Zhang et al., 2018). Hence, we hypothesized that *Vasn* deletion in osteoclasts might be responsible for the increased osteoclast activity in the long bones of complete *Vasn* KO mouse models. Surprisingly, the culture of primary *Vasn* KO osteoclasts on bone resorption plates did not reproduce the intense resorbing activity observed in *Vasn* KO mice. Moreover, the generation of mice with a specific deletion of *Vasn* in osteoclasts through a tamoxifen-inducible *Ctsk* promoter (Sanchez-Fernandez et al., 2012) was not associated with an altered long bone phenotype. Taken together, these data suggest that the deletion of *Vasn* in osteoclasts solely may not be sufficient to generate the bone alterations observed in the constitutive *Vasn* KO models.

Notch1 regulates osteoclast function, either directly by inhibiting precursor differentiation, or indirectly by increasing OPG/RANKL ratio and thus preventing resorption (Bai et al., 2008). Given that i) the Notch pathway was not altered in *Vasn* KO osteoclasts when cocultured with KO osteoblasts, and ii) *Vasn* KO osteoblasts released high amount of soluble RANKL whatever the Coculture condition, consistent with the strong osteoclast activity evidenced in complete *Vasn* KO models, this supports that the important osteoclast activity observed in these models was mainly due to the osteoblast lineage and its strong RANKL release. The absence of altered bone phenotype in *Vasn* KO mice with a targeted deletion of *Vasn* in osteoclasts further strengthen this hypothesis. The transwell culture system used here allows the passage of soluble cytokines but prevents direct cell contact, thus excluding the effect of membrane-bound cytokines (Mansouri et al., 2015). Membrane-bound RANKL has been shown to be important in bone pathophysiology (Asano et al., 2019; Xiong et al., 2018). This interaction is *de facto* not taken into account in our Coculture model and this is a limitation of our study. However, the choice of this transwell system (Mansouri

et al., 2015) seems relevant here since we found 1) an increased release in soluble RANKL by *Vasn* KO osteoblasts, 2) that the Notch pathway, which modulates the RANK-RANKL-OPG system through the release of soluble RANKL (Irtyuga et al., 2017; Padovano et al., 2023; Yamada et al., 2003), is inhibited in *Vasn* KO osteoblasts. Future studies are needed to investigate the role of *Vasn* on membrane bound-RANKL.

The YAP1-ECM axis and the regulatory circuits of the STAT3 pathway, two important signaling pathways for osteoclast activity (Y. Yang et al., 2019; Zhao et al., 2018), were changed in *Vasn* KO osteoclasts. Interestingly, both pathways are known to be involved in osteoclast differentiation and maturation through dialog with osteoblasts (Y. Chen et al., 2020; Xue et al., 2022; W. Yang et al., 2018; Zhao et al., 2018). Hence, when cocultured with *Vasn* KO osteoblasts, *Vasn* KO osteoclasts exhibited striking gene expression changes related to these two signaling pathways as well as STAT3 activation at the protein level. Furthermore, the expression of genes directly related to the osteoclast resorbing activity, namely *MMP-9*, *Acp5* encoding for TRAP, and *Ctsk*, and to the ATP6i complex, the osteoclast proton pump that acidifies the bone lacunae (Boyle et al., 2003), was strongly upregulated in *Vasn* KO osteoclasts. Strengthening these data, TRAP staining revealed large osteoclasts with robust TRAP activity in double KO cultures. Taken together, our data demonstrate that the absence of *Vasn* is associated with an upregulation of osteoclast activity and, to a lesser degree, of osteoblast formation activity, resulting in an unbalance of bone turnover in favor of resorption. In the future, it appears relevant to develop double Cre *Vasn* KO mice targeting both osteoblasts and osteoclasts to investigate more in-depth the direct role of *Vasn* in bone pathophysiology.

In addition to osteoblasts and osteoclasts, osteocytes are the third type of bone cells critical for bone function, particularly the remodeling process (Bonewald, 2011; Delgado-Calle & Bellido, 2022; Qin et al., 2020). Here, ultrastructure analyses did not reveal abnormal osteocyte morphology in the absence of *Vasn*. However, the facts that osteocytes (i) derive from the osteoblasts, (ii) secrete RANKL, which is upregulated in *Vasn* KO osteoblasts, (iii) regulate the Wnt signaling pathway, which is altered in *Vasn* KO osteoblasts, by secreting sclerostin, point the need for future investigations on the role of *Vasn* in osteocytes under normal and pathological conditions.

FIGURE 7 Impact of osteoblast and osteoclast co-cultures on *Vasn* KO osteoblasts. (a) Experimental schematic representation of osteoblast (OB) and osteoclast (OC) co-cultures. OB were plated in transwell and cultured under osteogenic conditions for 10 days before contact with bone marrow derived monocytes. Bone marrow derived monocytes were plated on resorption plates and cultured under osteoclastic conditions without RANKL for 10 days with the transwell. We tested four conditions (1) OB WT/OC WT, (2) OB WT/OC *Vasn* KO, (3) OB *Vasn* KO/OC WT and (4) OB *Vasn* KO/OC *Vasn* KO. (b) At 10 days of Coculture, gene expression related to the WNT/ β -catenin pathway (*Tcf1* and *Lef1*), osteoblast differentiation (*Runx2*, *AlpL*, *Col2A1*), TGF- β pathway (*TGF- β 1*), Notch pathway (*Hes1*, *HeyL*), STAT3 pathway (*Stat3*), cytokines regulating the osteoclast differentiation (*RankL*, *Opg*, *Il-6*) and *Vasn* was explored in OBs by RT-qPCR. Results are expressed as mean fold change ($\Delta\Delta CT$) \pm SD. * represents a significant difference (* $p < 0.05$, ** $p < 0.01$, *** $p < 0.001$) between control (OB WT/OC WT). (c) Western blot analysis showing higher activation of the β -Catenin in the double *Vasn* KO group compared to WT. This observation was confirmed by quantification of the blots ($n = 4$). Results are expressed as mean \pm SD. * represents a significant difference * $p < 0.05$.

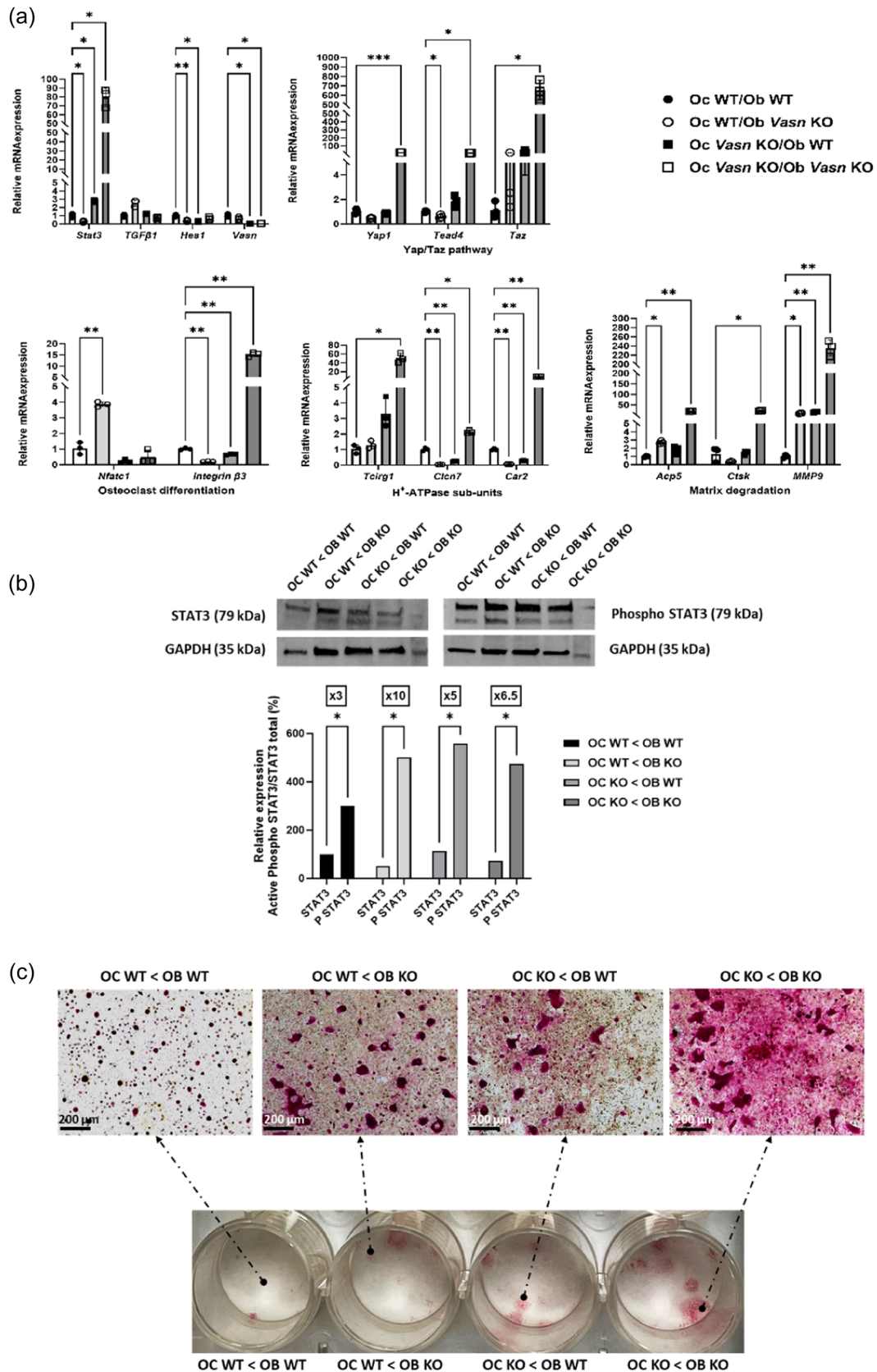


FIGURE 8 (See caption on next page).

In conclusion, the presence of *Vasn* in the two main cell lineages regulating bone resorption unravels a direct role of *Vasn* in bone pathophysiology. This protein interferes with the osteoclast-osteoblast dialog through several signaling pathways including Wnt/ β -catenin (Figure 9b). This indicates that *Vasn* must be recognized as a significant actor in the complex process governing osteoclastic bone resorption. These findings urge the need for more in-depth investigations on *Vasn* by generating preclinical models with deletion in both osteoblasts and osteoclasts. Overall, this study suggests that *Vasn* may be a biomarker for bone disorders, especially those with an imbalance in the osteoblast and osteoclast interplay, or constitute a therapeutic target for such disorders.

4 | MATERIALS AND METHODS

4.1 | Ethical approval and animal management

All animal experiments were performed according to a protocol approved by the Animal Care Committee of Université Paris Cité (project agreement 15-009, APAFIS #6173 N°2015112518204933). The mice were maintained according to the guidelines for ethical conduct developed by the Animal Care Committee of French Veterinary Services (DDPP Haut de Seine, France: agreement number C92-049-01). All efforts were made to minimize their pain and discomfort.

4.2 | Mice

All mice were housed under stable conditions (22°C \pm 2°C) with a 12-h-dark/light cycle, and with ad libitum access to water and standard pelleted food. For all the mouse strains, both sexes were analyzed indifferently.

4.2.1 | Constitutive *Vasn* knock-out mice (constitutive *Vasn* KO)

Heterozygous *Vasn*^{null} (*Vasn* HZ) mice were provided by Heinrich Schrewe (Max Planck Institute for Molecular Genetics, Berlin, Germany). Heterozygous breeding was carried out to generate homozygous *Vasn*^{null/null} (*Vasn*-null) mice. Tail snips were collected

for genotyping, DNA was extracted using DirectPCR (Viagen Biotech) and the genotype was determined by PCR using primers for the *Vasn* gene (Supporting Information S1: Table S1).

4.2.2 | Inducible *Vasn* knock-out mice (inducible *Vasn* KO)

Conditional *Vasn*^{flox} knock-out mice were mated with inducible general Cre deleter transgenic mice (CAGGCre-ERTM; Jackson Laboratory, #004682) to generate tamoxifen-inducible *Vasn* KO mice (*Vasn*^{flox/flox}; CAGGCre-ERTM). Genotype was determined by PCR using primers for the *Vasn* and the Cre recombinase gene (Supporting Information S1: Table S1). Cre-activation by tamoxifen (Sanchez-Fernandez et al., 2012) consisted of intraperitoneal injections of tamoxifen 20 mg/mL (100 μ L/mice) (Merck KGaA) suspended in sterile peanut oil (Merck KGaA) for five consecutive days (n = 6 mice per group). Mice received tamoxifen injections at 8 weeks of age. In parallel, age-matched inducible *Vasn* KO mice were injected with vehicle (peanut oil) for five consecutive days and used as control.

4.2.3 | Inducible osteoclast-specific *Vasn* knock-out mice

Conditional *Vasn*^{flox} knock-out mice were mated with cathepsin K-CreERT2 (*Ctsk*-cre/ERT2) mice (Sanchez-Fernandez et al., 2012) to generate tamoxifen-inducible osteoclast-specific *Vasn*-deficient mice (*Vasn*^{flox/flox}; *Ctsk*-cre/ERT2) mice. Genotype was determined by PCR using primers for the *Ctsk* and Cre recombinase genes, as well as *Vasn* (Supporting Information S1: Table S1). Cre-activation by tamoxifen injection and vehicle injection followed the same protocol/procedure as for the inducible *Vasn* KO model.

4.3 | Growth parameters

4.3.1 | X-ray microcomputed tomography analysis

Wild type (WT) and constitutive *Vasn* KO mice were scanned at post-natal day 21 (D21) using a high-resolution X-ray microcomputed tomography (μ CT system) (Quantum FX Caliper, Life Sciences, Perkin Elmer) hosted by the PIV facility (URP2496). Standard acquisition

FIGURE 8 Impact of osteoblast and osteoclast co-cultures on *Vasn* KO osteoclasts. At 10 days of Coculture, (a) gene expression related to TGF- β pathway (*TGF- β 1*), Notch pathway (*Hes1*), STAT3 pathway (*Stat3*), YAP/TAZ pathway (*Yap*, *Tead4*, *Taz*), osteoclast differentiation (*Nfatc1*, *Integrin β 3*), osteoclast resorption activity (*Acp5* (TRAP), *Ctsk*, *MMP9*, *Tcrg1*, *Clcn7*, *Car2*) and *Vasn* was explored in OCs by RT-qPCR. Results are expressed as mean fold change ($\Delta\Delta$ CT) \pm SD. * represents a significant difference (* p < 0.05, ** p < 0.01, *** p < 0.001) between control (OB WT/OC WT) and the different conditions. (b) Western blot analysis showing significant activation of the STAT3 pathway in all the groups. This observation was confirmed by quantification of the blots for the PSTAT3/STAT3 ratio (n = 3). Results are expressed as mean \pm SD. * represents a significant difference * p < 0.05. (c) TRAP staining showing positive cells for all the conditions. Osteoclasts were larger and the staining was particularly strong in the OB KO/OC KO condition compared to the other conditions (n = 3).

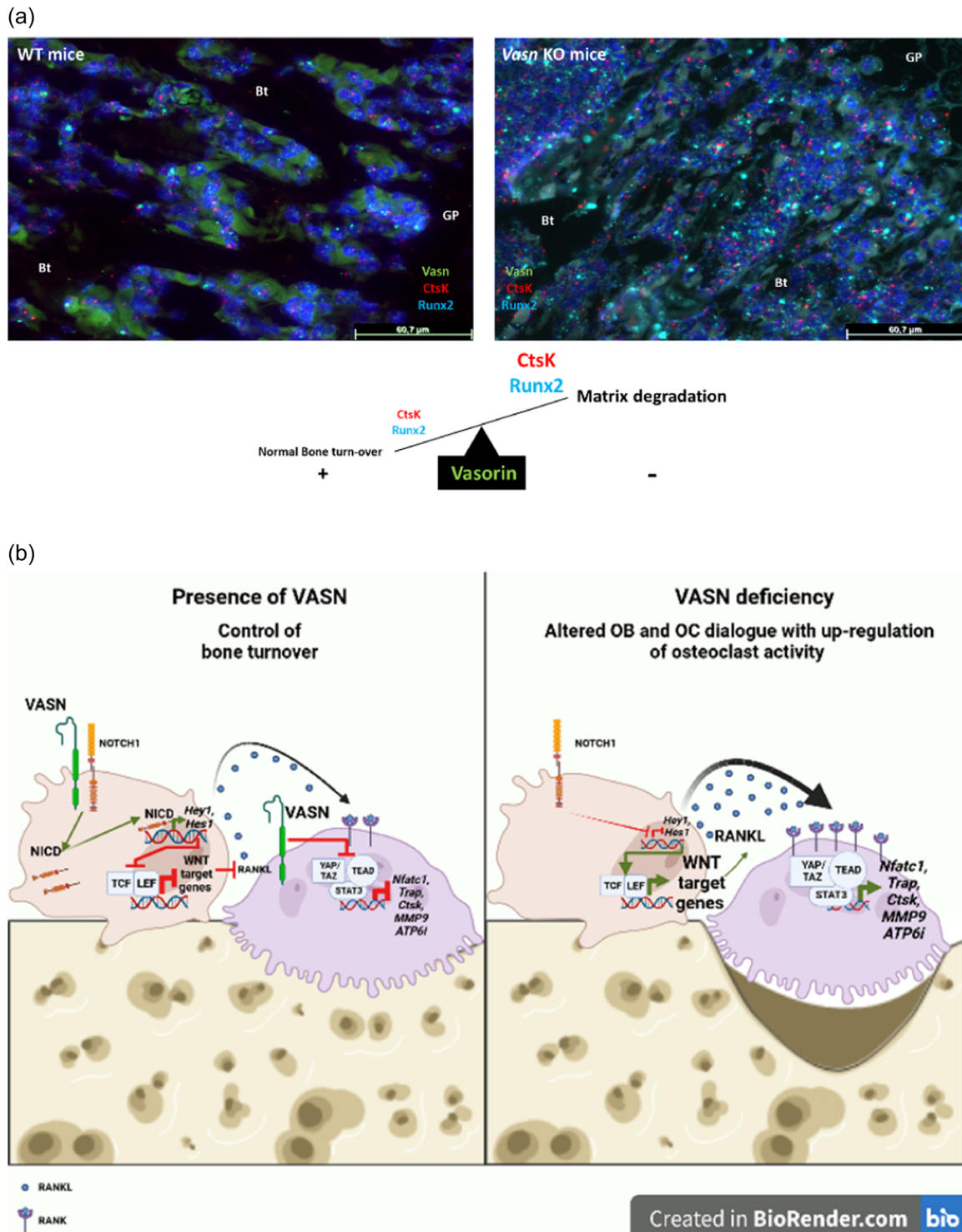


FIGURE 9 Role of vadorin in bone turnover. (a) RNA-scope on femurs sampled in 21-day-old WT and *Vasn* KO mice. We used *Vasn*, *Runx2* and *CtsK* fluorescent probes revealing that there is an increase in *Runx2* (Cyan dots) and *CtsK* (Red dots) RNA expression in the cells associated to bone trabeculae (Bt) located under the growth plate (GP) when mice are *Vasn* KO compared to WT (*Vasn* RNA in green). (b) Schematic representation of *Vasn* function in bone turnover. Left panel: In osteoblasts, *Vasn* can bind its NOTCH1 coreceptor allowing NOTCH1 cleavage and NICD internalization into the nucleus. As a transcription factor, NICD initiates transcription of NOTCH1 target genes such as *Hey1* and *Hes1*. Both HEY1 and HES1 act as inhibitors of the WNT signaling pathway when linked to TCF and LEF. This leads to a decrease in soluble RANKL release and, consequently, in osteoclast recruitment. In osteoclasts, *Vasn* acts as an inhibitor of the YAP/TAZ/STAT3 complex known to inhibit osteoclast differentiation and activity by decreasing the transcription of the genes encoding NFATc1, TRAP, CTSK, MMP9 and ATP6i complex. Right panel: In osteoblasts, when *Vasn* is deficient, there is no negative control of *Hey1* and *Hes1* transcription, resulting in an increase in WNT target genes transcription and consequent RANKL release. Consequently, there is an increase in osteoclast recruitment. In osteoclasts, there is no negative control of the YAP/TAZ/STAT3 complex formation resulting in enhanced expression of genes related to osteoclast activity. This dual effect of *Vasn* deletion in the osteoblast and osteoclast results in an imbalance of bone turnover in favor of osteoclast activity, resulting in increased bone resorption.

settings were applied (setting the voltage at 90 kV and intensity at 160 μ A), and scans were performed with a field of view focused on the growth plate and femur or covering the whole body. For bone exploration, mice were anesthetized (isoflurane, induction at 3%–4% under airflow of 0.8–1.5 L/min; 1.5%–2% under 400–800 mL/min thereafter). Tridimensional images were acquired with an isotropic voxel size of 20 μ m. Quantification of bone remodeling was performed using CTan Analyzer software (Skyscan, release 1.13.5.1). Trabecular bone was analyzed at the distal metaphysis of the femur drawing a volume of interest (VOI) by interpolation of 2D region at a 200 μ m height below the growth plate. The obtained interpolated VOI comprised bone trabeculae under growth plate area. A global threshold was determined interactively for bone selection to eliminate background noise. The following parameters were used: bone volume/total volume (BV/TV) ratio, trabecular number (Tb.N), trabecular separation (Tb. Sp), and trabecular thickness (Tb. Th). The cortical was analyzed at the middle of the femur (C. th) (Bouxsein et al., 2010). Bone reconstruction was performed with Osirix 5.8 viewer software (Pixmeo).

4.3.2 | Histology and histomorphometry

Mice were killed for histological analysis at D21 for constitutive *Vasn* KO mice and at D22 after injection for inducible *Vasn* KO mice. Femurs were fixed overnight at 4°C in 70% ethanol solution and dehydrated in a graded ethanol series.

Non-demineralized samples were fixed in 70% vol/vol ethanol (48 h at 4°C), dehydrated in graded ethanol solutions, and embedded at –20°C in methyl methacrylate resin (Merck) without decalcification. Resin-embedded femur samples were cut (5 μ m thick) using a Jung Polycut E microtome (Leica) with hard tissue blades (Leica). After immersion in a drop of 80% vol/vol ethanol, sections were stretched to a fold-free state on gelatin-coated glass slides (Menzel-Glaser, Thermofisher), covered with a polyethylene sheet, and tightly pressed on the glass slides, followed by overnight drying at room temperature (RT). Deplastification was carried out in 2-methoxyethyl acetate (Carlo Erba reagents) three times for 20 min. Rehydration of the sections was performed in graded ethanol solutions and then cleared in phosphate buffered solution for subsequent procedures. Image acquisition was performed using a DMLB Leica microscope, equipped with an imaging camera DFC425 Leica connected to the Leica application (LAS version 4.4).

4.3.3 | Mineral apposition rate

To label bone mineralization fronts, 2-month-old vehicle or tamoxifen induced *Vasn* KO mice were injected intraperitoneally with Calcein (Sigma-Aldrich, 30 mg/kg) at day 10 after tamoxifen or vehicle first injection and with Demeclocycline (Sigma-Aldrich, 30 mg/kg) at day 17 (24 h before sacrifice). Unstained methyl methacrylate sections (8 μ m thick) were used to measure the distance between the 2

labeled fronts, which constitutes the mineral apposition rate (MAR) (Parfitt et al., 1987). MAR was analyzed on a microvision instruments microscope with cartograph and histolab software for image acquisition and quantification (microvision instruments).

4.3.4 | Transmission electron microscopy

Femurs of constitutive *Vasn* KO, inducible *Vasn* KO and WT mice were analyzed by conventional transmission electron microscopy (TEM) to see osteoclast, osteoblast and osteocyte ultrastructure. Samples were fixed in 4% paraformaldehyde, demineralized in a sodium cacodylate buffer 0.06 M, pH 7.4 containing 1.9% Glutaraldehyde and 0.15 M EDTA at 4°C until complete decalcification. After post-fixation in 2% OsO₄ for 1 h and dehydration in graded ethanol series at 4°C, samples were embedded in Epon 812 (Fluka, Honeywell). Ultrathin sections of decalcified femurs were stained with uranyl acetate and lead citrate and were examined with a JEOL 1011 electron microscope.

4.3.5 | Enzyme histochemistry

Tartrate-resistant acid phosphatase (TRAP) was used to assess osteoclast activity by using 2.5 mM naphthol-ASTR-phosphate (Merck KGaA), 0.36 M N-N-dimethyl-formamide (Merck KGaA), and 4 mM salt in pH 5.2 acetate buffer. Non-osteoclastic acid phosphatase activity was inhibited with 100 mM L (+)-tartaric acid (Merck KGaA) added to the substrate solution for 1 h at 37°C. A count of the resorbed area relative to the total available trabecular bone area (Oc. S/BS) was performed within the secondary spongiosa. Only osteoclasts in contact with the bone surface and with an underlying bone gap were included in the count. Image acquisition was performed using a DMLB Leica microscope equipped with an imaging camera DFC425 Leica connected to the Leica application (LAS version 4.4).

Alkaline phosphatase (ALP) was used to reveal the layer of osteogenic cells by incubating the sections with naphthol ASTR phosphate (Merck KGaA) and diazonium fast blue RR salt (Merck KGaA, Darmstadt, Germany) for 30 min at 37°C (pH 9) in the presence of MgCl₂. Image acquisition was performed using a DMLB Leica microscope equipped with an imaging camera DFC425 Leica connected to the Leica application (LAS version 4.4).

4.3.6 | RNA-scope

The target genes and probed regions are available on Advanced Cell Diagnosis web site and designed for *mus musculus Vasn*, *CtsK* and *Runx2*. Sequences of target probes, preamplifier, amplifier, and label probe are proprietary (Advanced Cell Diagnostics, Hayward, CA). For fluorescent detection, the label probe was conjugated to OPAL 520, 570 and 690. (Advanced Cell Diagnostics, Hayward, CA). Paraffin

embedded tissue sections in 5- μ m thickness were deparaffinized in toluene, followed by dehydration in an ethanol series. Tissue sections were then incubated in EDTA buffer (1.21 g trisbase, 0.37 g EDTA titriplex III 0.5 ml Tween 20, H₂O qsp 1 L pH 9) maintained at 90°C using a hot plate for 5 min, rinsed in deionized water, and immediately treated with 10 μ g/mL protease (Advanced Cell Diagnostics, Hayward, CA) at 40°C for 30 min in a HybEZ hybridization oven (Advanced Cell Diagnostics, Hayward, CA). FFPE tissues were then incubated in order at 40°C with the following solutions: target probes in hybridization buffer A [6 \times SSC (1 \times SSC is 0.15 mol/L NaCl, 0.015 mol/L Na-citrate), 25% formamide, 0.2% lithium dodecyl sulfate, blocking reagents] for 3 h; preamplifier (2 nmol/L) in hybridization buffer B (20% formamide, 5 \times SSC, 0.3% lithium dodecyl sulfate, 10% dextran sulfate, blocking reagents) for 30 min; amplifier (2 nmol/L) in hybridization buffer B at 40°C for 15 min; and label probe (2 nmol/L) in hybridization buffer C (5 \times SSC, 0.3% lithium dodecyl sulfate, blocking reagents) for 15 min. After each hybridization step, slides were washed with wash buffer (0.1 \times SSC, 0.03% lithium dodecyl sulfate) three times at room temperature. For multiplex detection, equimolar amounts of target probes, preamplifier, amplifier, and label probe of each amplification system were used. Assays using archival paraffin embedded specimens were typically performed in parallel with positive and negative controls, to ensure interpretable results. The endogenous housekeeping gene *Ubc*, *Ppib* and *Polr2a* was used as positive control to assess both tissue RNA integrity and assay procedure. Positive staining with signals easily visible under a 10 \times objective lens was considered to be adequate. The bacterial gene *dapB* was used as negative control to assess background signals; completely negative staining was routinely achieved using our standard protocol.

4.3.7 | Blood parameters

All samples were collected via exsanguination by puncture of the retro-orbital sinus after anesthetizing the animals with isoflurane (induction at 3%–4% under airflow of 0.8–1.5 L/minute; 1.5%–2% under 400–800 mL/minute thereafter) into heparin tubes.

Serum 1,25-dihydroxyvitamin D

The samples were allowed to clot at RT. The serum was collected after centrifugation at 100 \times g for 15 min and stored at –20 °C. 1,25 dihydroxycholecalciferol levels were evaluated at the Erasmus Medical Center (Rotterdam, The Netherlands) using the Gamma-B 1,25-dihydroxyvitamin D RIA (IDS, Boldon, UK) according to the manufacturer's instructions. Cross-reactivity with the inactive precursor, 25-hydroxyvitamin D, is 0.001% for this test.

Serum calcium, phosphate and alkaline phosphatase

The serum was collected after centrifugation at 100 g for 15 min and stored at –20°C. All parameters were evaluated by the biochemistry platform in the CRI UMR1149 (UFR Medecine, Bichat Hospital, Paris, France) on a BeckmanCoulter AU480.

4.3.8 | Cell cultures

Osteoblasts

Primary osteoblasts were isolated from the calvariae of 4-day-old WT and constitutive *Vasn* KO mice. Calvariae were sequentially digested for 2 \times 7 min in 4 mM of EDTA and 1 \times 7 min of 2 mg/mL of type IV collagenase (Merck KGaA, Darmstadt, Germany) to remove fibroblasts and for 2 \times 30 min of 2 mg/mL of type IV collagenase to collect osteoblast progenitors. Cells were expanded for 5–6 days in minimum essential medium α (Gibco, Thermo Fisher Scientific) containing 10% fetal bovine serum and plated at 100,000 cells per well in 6-well plate for alkaline phosphatase and alizarin red assay or 25,000 cells per well in 24-well plates for total RNA extraction. At this point, the medium was supplemented with 10^{–8}M of dexamethasone, 50 μ g/mL of ascorbic acid and 10 mM of β -glycerophosphate (Merck KGaA, Darmstadt, Germany), and was replaced every 2–3 days until 7, 14 and 21 days for the determination of alkaline phosphatase activity and alizarin red quantification or until 14 days for total RNA extraction.

Osteoclasts

Bone marrow (BM) derived monocytes were aseptically collected from the femur and tibia from WT and constitutive *Vasn* KO mice, depleted of red blood cells with Leukocyte Separation Medium (Corning) and plated at 200,000 cells per well in 24-well resorption plate (Cosmo bio co ltd, Carlsbad, CA) or plastic for total RNA extraction and TRAP staining. Cells were plated at 20,000 cells per well in a 96-well plate on a bone slice (IDS, PerkinElmer UK) for quantification of surface and depth resorption. On day one, osteoclast differentiation was induced with 25 ng/mL of rmM-CSF and 50 ng/mL of rmRANKL (Bio-Techne) on plastic or 100 ng/mL of rmRANKL on resorption plate or bone slice. Medium was changed every 2 days until day 7 or 10 days.

Coculture of osteoblasts and osteoclasts

WT and *Vasn* KO osteoblast and osteoclast progenitors were harvested using the methods described above. Osteoblast differentiation was first induced in a cell culture insert 1.0 μ m pore size (Transwell Inserts Falcon, Durham NC) with 10^{–8} M of dexamethasone, 50 μ g/mL of ascorbic acid and 10 mM of β -glycerophosphate. At 10 days after induction, osteoclast precursors were plated on the bone resorption plate of the coculture system for 10 days under osteoclastic differentiation conditions (rmM-CSF 50 ng/mL and no RANKL which was produced by osteoblasts) (Figure 7a).

Scanning electron microscopy

Bone slices were dehydrated with 100% ethanol for 1 h at room temperature, then metalized with a gold/platinum alloy in a metalizer (Biorad, Hercules), and visualized with a scanning electron microscope Jeol jsm-6400. Surface of resorption was quantified with ImageJ software.

Quantification of resorption pit depth

Bone slices were treated for 10 min with 10% of bleaching water to remove cells of the surface. After water rinse, bone slices were visualized with a 2-photon SP8 dive flim (Leica) using reflection of 488 nm lasers and a z acquisition. Two measures of the z-axis profile were realized: one on top of the bone surface, a second on the bottom of the resorption pit, with ImageJ software. The depth of each pit was obtained by calculating the delta between these two points.

Quantitative analysis of alizarin red staining

Cells were fixed in 4% paraformaldehyde for 15 min at room temperature and stained for 30 min with 2% alizarin red stain (ARS) solution (Merck KGaA, Darmstadt, Germany) at a pH level of 4.2 under gentle agitation. The cells were washed 3 times with distilled water and viewed under a light microscope, followed by dry extraction of the stain for colorimetric quantification. For quantification of staining, 800 μ L 10% (v/v) acetic acid was added to each well, and the plate was incubated at room temperature for 30 min with shaking. The monolayer, now loosely attached to the plate, was then scraped from the plate with a cell scraper and transferred to a 1.5-mL microcentrifuge tube. After vortexing for 30 s, the slurry was overlaid with 500 μ L glycerol, heated to exactly 85°C for 10 min, and transferred to ice for 5 min. The slurry was centrifuged at 20,000 g for 15 min, and 500 μ L of the supernatant was removed to a new 1.5-mL microcentrifuge tube. Then 200 μ L of 10% (v/v) ammonium hydroxide was added to neutralize the acid. Aliquots (150 μ L) of the supernatant were read in triplicate at 405 nm in 96-well format.

Multiplex immunoassay

Osteoblast supernatants were collected at Day 0, 7, 14 and 21 and analyzed with the Bioplex200 device from BioRad (Hercules, CA) using a mouse magnetic Luminex assay plate (Bio-Techne, Minneapolis, MN). The panel included RANKL, M-CSF, VEGF, IL-6, osteopontin and IL-1 β . Each supernatant was assayed in duplicate, with the average value taken as a result. The unit for all the cytokines measured in this study is pg/mL.

RT-qPCR

Total RNA was isolated using TRIzol reagent (Invitrogen). Reverse transcription was performed with random primers using Verso cDNA Synthesis Kit (Thermo Fisher Scientific, Waltham, MA). Real-time Quantitative PCR was then performed using primers listed below and LightCycler 480 SYBR Green I Master (Roche Applied Science, IN) on LightCycler 96 (Roche Applied Science, IN). Actin served as house-keeping gene. Fold changes were normalized using the $\Delta\Delta$ Ct formula (primers in Supporting Information S1: Table S1).

mRNA sequencing

After RNA extraction, RNA concentrations were obtained using nanodrop or a fluorometric Qubit RNA assay (Life Technologies). The quality of the RNA (RNA integrity number) was determined on the Agilent 2100 Bioanalyzer (Agilent Technologies) as per the

manufacturer's instructions. To construct the libraries, 1 μ g of high-quality total RNA sample (RIN > 8) was processed using TruSeq Stranded mRNA kit (Illumina) according to manufacturer instructions. Briefly, after purification of poly-A-containing mRNA molecules, mRNA molecules are fragmented and reverse-transcribed using random primers. Replacement of dTTP by dUTP during the second strand synthesis will permit to achieve the strand specificity. The addition of a single A base to the cDNA is followed by the ligation of Illumina adapters. Libraries were quantified by qPCR using the KAPA Library Quantification Kit for Illumina Libraries (KapaBiosystems) and library profiles were assessed using the DNA High Sensitivity LabChip kit on an Agilent Bioanalyzer. Libraries were sequenced on an Illumina Nextseq. 500 instrument using 75 base-lengths read V2 chemistry in a paired-end mode. After sequencing, a first analysis based on AOZAN software (ENS, Paris) was applied to demultiplex and control the raw data quality (based on FastQC modules/version 0.11.5). Obtained fastq files were then aligned using STAR algorithm (version 2.5.2b) and quality control of the alignment was realized with Picard tools (version 2.8.1). Reads were then counted using Featurecount (version Rsubread 1.24.1) and the statistical analyses on the read counts were performed with the DESeq. 2 package version 1.14.1 to determine the proportion of differentially expressed genes between two conditions.

Western blot

Cells were treated with (RIPA) lysis buffer, separated by SDS-polyacrylamide gel electrophoresis, and transferred to nitrocellulose membranes that were incubated with primary antibodies against active b-catenin (1:1000, ab652504/Abcam) or against STAT3 or phosphor STAT3 (Cell signaling, Danvers, MA) or Gapdh antibody (1:1000, Proteintech) overnight at 4°C and secondary antibody (Dako) at room temperature for 1 h and visualized by using Clarity Western ECL Substrate (BioRad). Chemiluminescent signals were detected with the BioRad Imaging System. Quantifications were realized using ImageJ Software.

STATISTICAL ANALYSIS

Statistical analyses were carried out, and graphs were plotted with GraphPad Prism, version 7.0. The distribution of variables was tested with Kolmogorov-Smirnov test. Normality and lognormality were tested with Shapiro-Wilk test. For continuous variables, comparisons were performed using ANOVA and results were expressed as mean \pm SD. When data were not continuous, comparisons were performed using Mann-Whitney test and results were expressed as mean \pm SD. *p*-values of less or equal to 0.05 were considered significant.

ILLUSTRATIONS

All figure illustrations were created with BioRender. com.

AUTHOR CONTRIBUTIONS

Conceptualization: Catherine Chaussain, Celine Gaucher, Claire Bardet, Heinrich Schrewe, Pierre Louis Tharaux. **Methodology:** Catherine Chaussain, Caroline Andrique, Anne Laure Bonnet, Julie Lesieur. **Investigation:** Caroline Andrique, Anne Laure Bonnet, Julie Lesieur, Jeremy Sadoine, Coralie Torrens, Brigitte Baroukh, A. Michae-la Krautzberger, Julien Dang. **Visualization:** Caroline Andrique, Anne Laure Bonnet, Catherine Chaussain. **Supervision:** Catherine Chaussain, Celine Gaucher, Heinrich Schrewe. **Writing—original draft:** Catherine Chaussain, Caroline Andrique, Anne Laure Bonnet. **Writing—review and editing:** Caroline Andrique, Anne Laure Bonnet, Julien Dang, Julie Lesieur, Gael Y. Rochefort, Isabelle Six, Pascal Houillier, Heinrich Schrewe, Celine Gaucher, Catherine Chaussain.

ACKNOWLEDGMENTS












This work was supported by Université Paris Cité, by the *Agence Nationale de la Recherche* (grant 17-CE14-0028), and the *Fondation pour la Recherche Médicale* (grant DGE20111123012).

We do thank Bernard Hoflack (Biotechnologisches Zentrum, TU-Dresden, Dresden, Germany) for providing the inducible *CathepsinK-Cre* mouse model. We are grateful to Stéphane Le Goff (UEB2i, Université Paris Cité) for his assistance with SEM, Thomas Guilbert (Imagic Institut Cochin, Université Paris Cité) for his assistance with the confocal microscopy, Niclas Setterblad (IRSL) for his help with cell characterization, and Juliette Hamroune, Lucie Adoux and Benjamin Saint Pierre (Genomic Institut Cochin, Université Paris Cité) for the RNA sequencing and analysis. We do thank Dr Pierre Jurdic (Université de Lyon) and Prof Jean Louis Saffar (Université Paris Cité) for helpful discussion regarding bone pathophysiology with their invaluable expertise. In vivo imaging was performed at the Life Imaging Facility of Université Paris Cité (Plateforme Imageries du Vivant), supported by France Life Imaging (grant ANR-11-INBS-0006) and Infrastructures Biologie-Santé.

CONFLICT OF INTEREST STATEMENT

All other authors declare they have no competing interests.

ORCID

Caroline Andrique  <http://orcid.org/0000-0002-0447-9616>
 Anne Laure Bonnet  <https://orcid.org/0000-0003-2261-0216>
 Julien Dang  <https://orcid.org/0000-0002-5690-7424>
 Julie Lesieur  <https://orcid.org/0000-0002-5981-3458>
 Jeremy Sadoine  <https://orcid.org/0000-0003-4809-3018>
 Gael Y. Rochefort  <https://orcid.org/0000-0001-6428-3570>
 Claire Bardet  <https://orcid.org/0000-0002-0874-4843>
 Isabelle Six  <http://orcid.org/0000-0002-5256-8138>
 Pierre Louis Tharaux  <https://orcid.org/0000-0002-6062-5905>
 Celine Gaucher  <https://orcid.org/0000-0002-5530-8163>
 Catherine Chaussain  <https://orcid.org/0000-0002-3463-3936>

REFERENCES

- Ahn, J. M., Kim, B. G., Yu, M. H., Lee, I. K., & Cho, J. Y. (2010). Identification of diabetic nephropathy-selective proteins in human plasma by multi-lectin affinity chromatography and LC-MS/MS. *PROTEOMICS - Clinical Applications*, 4(6-7), 644-653. <https://doi.org/10.1002/prca.200900196>
- Asano, T., Okamoto, K., Nakai, Y., Tsutsumi, M., Muro, R., Suematsu, A., Hashimoto, K., Okamura, T., Ehata, S., Nitta, T., & Takayanagi, H. (2019). Soluble RANKL is physiologically dispensable but accelerates tumour metastasis to bone. *Nature Metabolism*, 1(9), 868-875. <https://doi.org/10.1038/s42255-019-0104-1>
- Bai, S., Kopan, R., Zou, W., Hilton, M. J., Ong, C., Long, F., Ross, F. P., & Teitelbaum, S. L. (2008). NOTCH1 regulates osteoclastogenesis directly in osteoclast precursors and indirectly via osteoblast lineage cells. *Journal of Biological Chemistry*, 283(10), 6509-6518. <https://doi.org/10.1074/jbc.M707000200>
- Balakrishnan, L., Nirujogi, R. S., Ahmad, S., Bhattacharjee, M., Manda, S. S., Renuse, S., Kelkar, D. S., Subbannayya, Y., Raju, R., Goel, R., Thomas, J. K., Kaur, N., Dhillon, M., Tankala, S. G., Jois, R., Vasdev, V., Ramachandra, Y., Sahasrabudhe, N. A., Prasad, T. K., ... Pandey, A. (2014). Proteomic analysis of human osteoarthritis synovial fluid. *Clinical Proteomics*, 11(1), 6. <https://doi.org/10.1186/1559-0275-11-6>
- Ballhause, T. M., Jiang, S., Baranowsky, A., Brandt, S., Mertens, P. R., Frosch, K. H., Yorgan, T., & Keller, J. (2021). Relevance of notch signaling for bone metabolism and regeneration. *International Journal of Molecular Sciences*, 22(3), 1325. <https://doi.org/10.3390/ijms22031325>
- Baron, R., & Kneissel, M. (2013). WNT signaling in bone homeostasis and disease: From human mutations to treatments. *Nature Medicine*, 19(2), 179-192. <https://doi.org/10.1038/nm.3074>
- Bonewald, L. F. (2011). The amazing osteocyte. *Journal of Bone and Mineral Research*, 26(2), 229-238. <https://doi.org/10.1002/jbmr.320>
- Bonnet, A. L., Chaussain, C., Broutin, I., Rochefort, G. Y., Schrewe, H., & Gaucher, C. (2018). From vascular smooth muscle cells to folliculogenesis: What about vasorin? *Frontiers in Medicine*, 5, 335. <https://doi.org/10.3389/fmed.2018.00335>
- Boskey, A. L., Gelb, B. D., Pourmand, E., Kudrashov, V., Doty, S. B., Spevak, L., & Schaffler, M. B. (2009). Ablation of cathepsin K activity in the young mouse causes hypermineralization of long bone and growth plates. *Calcified Tissue International*, 84(3), 229-239. <https://doi.org/10.1007/s00223-008-9214-6>
- Bouxsein, M. L., Boyd, S. K., Christiansen, B. A., Guldberg, R. E., Jepsen, K. J., & Müller, R. (2010). Guidelines for assessment of bone microstructure in rodents using micro-computed tomography. *Journal of Bone and Mineral Research*, 25(7), 1468-1486. <https://doi.org/10.1002/jbmr.141>
- Boyce, B. F., & Xing, L. (2008). Functions of RANKL/RANK/OPG in bone modeling and remodeling. *Archives of Biochemistry and Biophysics*, 473(2), 139-146. <https://doi.org/10.1016/j.abb.2008.03.018>
- Boyle, W. J., Simonet, W. S., & Lacey, D. L. (2003). Osteoclast differentiation and activation. *Nature*, 423(6937), 337-342. <https://doi.org/10.1038/nature01658>
- Canalis, E., Adams, D. J., Boskey, A., Parker, K., Kranz, L., & Zanotti, S. (2013). Notch signaling in osteocytes differentially regulates cancellous and cortical bone remodeling. *Journal of Biological Chemistry*, 288(35), 25614-25625. <https://doi.org/10.1074/jbc.M113.470492>
- Chambers, T. J. (2000). Regulation of the differentiation and function of osteoclasts. *The Journal of Pathology*, 192(1), 4-13. [https://doi.org/10.1002/1096-9896\(2000\)9999:9999::AID-PATH645>3.0.CO;2-Q](https://doi.org/10.1002/1096-9896(2000)9999:9999::AID-PATH645>3.0.CO;2-Q)
- Chen, L., Yao, J., Zhang, S., Wang, L., Song, H., & Xue, J. (2005). Slit-like 2, a novel zebrafish slit homologue that might involve in zebrafish central neural and vascular morphogenesis. *Biochemical and Biophysical Research Communications*, 336(1), 364-371. <https://doi.org/10.1016/j.bbrc.2005.08.071>
- Chen, Y., Wang, Y., Hu, J., Tang, Y., Tian, Z., Hu, W., Zeng, F., Tan, J., Dai, Q., Hou, Z., Luo, F., Xu, J., & Dong, S. (2020). Epthilone B

- prevents lipopolysaccharide-induced inflammatory osteolysis through suppressing osteoclastogenesis via STAT3 signaling pathway. *Aging*, 12(12), 11698–11716. <https://doi.org/10.18632/aging.103337>
- Cheng, X., Wan, Q. L., & Li, Z. B. (2017). AG490 suppresses interleukin-34-mediated osteoclastogenesis in mice bone marrow macrophages. *Cell Biology International*, 41(6), 659–668. <https://doi.org/10.1002/cbin.10771>
- Delgado-Calle, J., & Bellido, T. (2022). The osteocyte as a signaling cell. *Physiological Reviews*, 102(1), 379–410. <https://doi.org/10.1152/physrev.00043.2020>
- Engin, F., Yao, Z., Yang, T., Zhou, G., Bertin, T., Jiang, M. M., Chen, Y., Wang, L., Zheng, H., Sutton, R. E., Boyce, B. F., & Lee, B. (2008). Dimorphic effects of notch signaling in bone homeostasis. *Nature Medicine*, 14(3), 299–305. <https://doi.org/10.1038/nm1712>
- Guasto, A., & Cormier-Daire, V. (2021). Signaling pathways in bone development and their related skeletal dysplasia. *International Journal of Molecular Sciences*, 22(9), 4321. <https://doi.org/10.3390/ijms22094321>
- Hou, X., & Tian, F. (2022). STAT3-mediated osteogenesis and osteoclastogenesis in osteoporosis. *Cell Communication and Signaling*, 20(1), 112. <https://doi.org/10.1186/s12964-022-00924-1>
- Ikeda, Y., Imai, Y., Kumagai, H., Nosaka, T., Morikawa, Y., Hisaoka, T., Manabe, I., Maemura, K., Nakaoka, T., Imamura, T., Miyazono, K., Komuro, I., Nagai, R., & Kitamura, T. (2004). Vasorin, a transforming growth factor β -binding protein expressed in vascular smooth muscle cells, modulates the arterial response to injury in vivo. *Proceedings of the National Academy of Sciences*, 101(29), 10732–10737. <https://doi.org/10.1073/pnas.0404117101>
- Irtzya, O., Malashicheva, A., Zhiduleva, E., Freylikhman, O., Rotar, O., Bäck, M., Tarnovskaya, S., Kostareva, A., & Moiseeva, O. (2017). NOTCH1 mutations in aortic stenosis: Association with osteoprotegerin/RANK/RANKL. *BioMed Research International*, 2017, 1–10. <https://doi.org/10.1155/2017/6917907>
- Jann, J., Gascon, S., Roux, S., & Fauchoux, N. (2020). Influence of the TGF- β superfamily on osteoclasts/osteoblasts balance in physiological and pathological bone conditions. *International Journal of Molecular Sciences*, 21(20), 7597. <https://doi.org/10.3390/ijms21207597>
- Kleinhans, C., Schmid, F. F., Schmid, F. V., & Kluger, P. J. (2015). Comparison of osteoclastogenesis and resorption activity of human osteoclasts on tissue culture polystyrene and on natural extracellular bone matrix in 2D and 3D. *Journal of Biotechnology*, 205, 101–110. <https://doi.org/10.1016/j.jbiotec.2014.11.039>
- Koide, M., Yamashita, T., Nakamura, K., Yasuda, H., Udagawa, N., & Kobayashi, Y. (2022). Evidence for the major contribution of remodeling-based bone formation in sclerostin-deficient mice. *Bone*, 160, 116401. <https://doi.org/10.1016/j.bone.2022.116401>
- Kopan, R. (2012). Notch signaling. *Cold Spring Harbor Perspectives in Biology*, 4(10), a011213. <https://doi.org/10.1101/cshperspect.a011213>
- Kovar, H., Bierbaumer, L., & Radic-Sarikas, B. (2020). The YAP/TAZ pathway in osteogenesis and bone sarcoma pathogenesis. *Cells*, 9(4), 972. <https://doi.org/10.3390/cells9040972>
- Krautzbberger, A. M., Kosiol, B., Scholze, M., & Schrewe, H. (2012). Expression of vasorin (Vas) during embryonic development of the mouse. *Gene Expression Patterns*, 12(5–6), 167–171. <https://doi.org/10.1016/j.gexp.2012.02.003>
- Liang, W., Guo, B., Ye, J., Liu, H., Deng, W., Lin, C., Zhong, X., & Wang, L. (2019). Vasorin stimulates malignant progression and angiogenesis in glioma. *Cancer Science*, 110(8), 2558–2572. <https://doi.org/10.1111/cas.14103>
- Liang, W., Zuo, J., Liu, M., Su, Y., Guo, B., Hou, J., Xing, Q., Peng, Y., Fang, L., Cao, Y., Shan, J., Sun, R., Zhao, J., & Wang, J. (2023). VASN promotes colorectal cancer progression by activating the YAP/TAZ and AKT signaling pathways via YAP. *The FASEB Journal*, 37(1), e22688. <https://doi.org/10.1096/fj.202201181R>
- Liao, Z., Ke, W., Liu, H., Tong, B., Wang, K., Feng, X., Hua, W., Wang, B., Song, Y., Luo, R., Liang, H., Zhang, W., Zhao, K., Li, S., & Yang, C. (2022). Vasorin-containing small extracellular vesicles retard intervertebral disc degeneration utilizing an injectable thermoresponsive delivery system. *Journal of Nanobiotechnology*, 20(1), 420. <https://doi.org/10.1186/s12951-022-01624-1>
- Lin, G. L., & Hankenson, K. D. (2011). Integration of BMP, Wnt, and notch signaling pathways in osteoblast differentiation. *Journal of Cellular Biochemistry*, 112(12), 3491–3501. <https://doi.org/10.1002/jcb.23287>
- Liu, H., Kong, W., Wen, S., Wu, J., Yin, X., & Liu, Y. (2021). VASN promotes proliferation of laryngeal cancer cells via YAP/TAZ. *Journal of B.U.O.N.: Official Journal of the Balkan Union of Oncology*, 26(4), 1563–1570.
- Loftheim, H., Midtvedt, K., Hartmann, A., Reisæter, A. V., Falck, P., Holdaas, H., Jenssen, T., Reubsæet, L., & Åsberg, A. (2012). Urinary proteomic shotgun approach for identification of potential acute rejection biomarkers in renal transplant recipients. *Transplantation Research*, 1(1), 9. <https://doi.org/10.1186/2047-1440-1-9>
- Louvet, L., Lenglet, G., Krautzbberger, A. M., Mentaverri, R., Hague, F., Kowalewski, C., Mahtal, N., Lesieur, J., Bonnet, A. L., Andrique, C., Gaucher, C., Gomila, C., Schrewe, H., Tharaux, P. L., Kamel, S., Chaussain, C., & Six, I. (2022). Vasorin plays a critical role in vascular smooth muscle cells and arterial functions. *Journal of Cellular Physiology*, 237(10), 3845–3859. <https://doi.org/10.1002/jcp.30838>
- Man, J., Yu, X., Huang, H., Zhou, W., Xiang, C., Huang, H., Miele, L., Liu, Z., Bebek, G., Bao, S., & Yu, J. S. (2018). Hypoxic induction of vasorin regulates Notch1 turnover to maintain glioma stem-like cells. *Cell Stem Cell*, 22(1), 104–118.e6. <https://doi.org/10.1016/j.stem.2017.10.005>
- Mansouri, R., Haÿ, E., Marie, P. J., & Modrowski, D. (2015). Role of syndecan-2 in osteoblast biology and pathology. *BoneKey Reports*, 4, 666. <https://doi.org/10.1038/bonekey.2015.33>
- Moon, P. G., Lee, J. E., You, S., Kim, T. K., Cho, J. H., Kim, I. S., Kwon, T. H., Kim, C. D., Park, S. H., Hwang, D., Kim, Y. L., & Baek, M. C. (2011). Proteomic analysis of urinary exosomes from patients of early IgA nephropathy and thin basement membrane nephropathy. *Proteomics*, 11(12), 2459–2475. <https://doi.org/10.1002/pmic.201000443>
- Padovano, C., Bianco, S. D., Sansico, F., De Santis, E., Tamiro, F., Colucci, M., Totti, B., Di Iasio, S., Bruno, G., Panelli, P., Miscio, G., Mazza, T., & Giambra, V. (2023). The Notch1 signaling pathway directly modulates the human RANKL-induced osteoclastogenesis. *Scientific Reports*, 13(1), 21199. <https://doi.org/10.1038/s41598-023-48615-2>
- Pakvasa, M., Haravu, P., Boachie-Mensah, M., Jones, A., Coalson, E., Liao, J., Zeng, Z., Wu, D., Qin, K., Wu, X., Luo, H., Zhang, J., Zhang, M., He, F., Mao, Y., Zhang, Y., Niu, C., Wu, M., Zhao, X., ... Reid, R. R. (2021). Notch signaling: Its essential roles in bone and craniofacial development. *Genes & Diseases*, 8(1), 8–24. <https://doi.org/10.1016/j.gendis.2020.04.006>
- Parfitt, A. M., Drezner, M. K., Glorieux, F. H., Kanis, J. A., Malluche, H., Meunier, P. J., Ott, S. M., & Recker, R. R. (1987). Bone histomorphometry: Standardization of nomenclature, symbols, and units. Report of the ASBMR histomorphometry nomenclature committee. *Journal of Bone and Mineral Research*, 2(6), 595–610. <https://doi.org/10.1002/jbmr.5650020617>
- Ponzetti, M., & Rucci, N. (2021). Osteoblast differentiation and signaling: Established concepts and emerging topics. *International Journal of Molecular Sciences*, 22(13), 6651. <https://doi.org/10.3390/ijms22136651>
- Qin, L., Liu, W., Cao, H., & Xiao, G. (2020). Molecular mechanosensors in osteocytes. *Bone Research*, 8, 23. <https://doi.org/10.1038/s41413-020-0099-y>

- Raggatt, L. J., & Partridge, N. C. (2010). Cellular and molecular mechanisms of bone remodeling. *Journal of Biological Chemistry*, 285(33), 25103–25108. <https://doi.org/10.1074/jbc.R109.041087>
- Samavat, S., Kalantari, S., Nafar, M., Rutishauser, D., Rezaei-Tavirani, M., Parvin, M., & Zubarev, R. A. (2015). Diagnostic urinary proteome profile for immunoglobulin a nephropathy. *Iranian Journal of Kidney Diseases*, 9(3), 239–248.
- Sanchez-Fernandez, M. A., Sbacchi, S., Correa-Tapia, M., Naumann, R., Klemm, J., Chambon, P., Al-Robaiy, S., Blessing, M., & Hoflack, B. (2012). Transgenic mice for a tamoxifen-induced, conditional expression of the Cre recombinase in osteoclasts. *PLoS One*, 7(5), e37592. <https://doi.org/10.1371/journal.pone.0037592>
- Swiatek, P. J., Lindsell, C. E., del Amo, F. F., Weinmaster, G., & Gridley, T. (1994). Notch1 is essential for postimplantation development in mice. *Genes & Development*, 8(6), 707–719. <https://doi.org/10.1101/gad.8.6.707>
- Tanaka, S., & Matsumoto, T. (2021). Sclerostin: From bench to bedside. *Journal of Bone and Mineral Metabolism*, 39(3), 332–340. <https://doi.org/10.1007/s00774-020-01176-0>
- Tsukasaki, M., & Takayanagi, H. (2022). Osteoclast biology in the single-cell era. *Inflammation and Regeneration*, 42(1), 27. <https://doi.org/10.1186/s41232-022-00213-x>
- Udagawa, N., Koide, M., Nakamura, M., Nakamichi, Y., Yamashita, T., Uehara, S., Kobayashi, Y., Furuya, Y., Yasuda, H., Fukuda, C., & Tsuda, E. (2021). Osteoclast differentiation by RANKL and OPG signaling pathways. *Journal of Bone and Mineral Metabolism*, 39(1), 19–26. <https://doi.org/10.1007/s00774-020-01162-6>
- Xiong, J., Cawley, K., Piemontese, M., Fujiwara, Y., Zhao, H., Goellner, J. J., & O'Brien, C. A. (2018). Soluble RANKL contributes to osteoclast formation in adult mice but not ovariectomy-induced bone loss. *Nature Communications*, 9(1), 2909. <https://doi.org/10.1038/s41467-018-05244-y>
- Xue, Y., Zhao, C., & Liu, T. (2022). Interferon-induced protein with tetratricopeptide repeats 1 (IFIT1) accelerates osteoclast formation by regulating signal transducer and activator of transcription 3 (STAT3) signalling. *Bioengineered*, 13(2), 2285–2295. <https://doi.org/10.1080/21655979.2021.2024333>
- Yamada, T., Yamazaki, H., Yamane, T., Yoshino, M., Okuyama, H., Tsuneto, M., Kurino, T., Hayashi, S. I., & Sakano, S. (2003). Regulation of osteoclast development by Notch signaling directed to osteoclast precursors and through stromal cells. *Blood*, 101(6), 2227–2234. <https://doi.org/10.1182/blood-2002-06-1740>
- Yang, L., Cheng, X., Shi, W., Li, H., Zhang, Q., Huang, S., Huang, X., Wen, S., Gan, J., Liao, Z., Sun, J., Liang, J., Ouyang, Y., & He, M. (2022). Vasorin deletion in C57BL/6J mice induces hepatocyte autophagy through glycogen-mediated mTOR regulation. *Nutrients*, 14(17), 3600. <https://doi.org/10.3390/nu14173600>
- Yang, W., Han, W., Qin, A., Wang, Z., Xu, J., & Qian, Y. (2018). The emerging role of hippo signaling pathway in regulating osteoclast formation. *Journal of Cellular Physiology*, 233(6), 4606–4617. <https://doi.org/10.1002/jcp.26372>
- Yang, Y., Chung, M. R., Zhou, S., Gong, X., Xu, H., Hong, Y., Jin, A., Huang, X., Zou, W., Dai, Q., & Jiang, L. (2019). STAT3 controls osteoclast differentiation and bone homeostasis by regulating NFATc1 transcription. *Journal of Biological Chemistry*, 294(42), 15395–15407. <https://doi.org/10.1074/jbc.RA119.010139>
- Yu-Lee, L. Y., Lee, Y. C., Pan, J., Lin, S. C., Pan, T., Yu, G., Hawke, D. H., Pan, B. F., & Lin, S. H. (2019). Bone secreted factors induce cellular quiescence in prostate cancer cells. *Scientific Reports*, 9(1), 18635. <https://doi.org/10.1038/s41598-019-54566-4>
- Zanotti, S., & Canalis, E. (2013). Mechanisms in endocrinology: Notch signaling in skeletal health and disease. *European Journal of Endocrinology*, 168(6), R95–R103. <https://doi.org/10.1530/EJE-13-0115>
- Zanotti, S., Smerdel-Ramoya, A., Stadmeyer, L., Durant, D., Radtke, F., & Canalis, E. (2008). Notch inhibits osteoblast differentiation and causes osteopenia. *Endocrinology*, 149(8), 3890–3899. <https://doi.org/10.1210/en.2008-0140>
- Zhang, D., Jing, J., Lou, F., Li, R., Ping, Y., Yu, F., Wu, F., Yang, X., Xu, R., Li, F., Wang, K., Bai, M., Pi, C., Xie, J., Zheng, L., Ye, L., & Zhou, X. (2018). Evidence for excessive osteoclast activation in SIRT6 null mice. *Scientific Reports*, 8(1), 10992. <https://doi.org/10.1038/s41598-018-28716-z>
- Zhao, L., Guan, H., Song, C., Wang, Y., Liu, C., Cai, C., Zhu, H., Liu, H., Zhao, L., & Xiao, J. (2018). YAP1 is essential for osteoclastogenesis through a TEADs-dependent mechanism. *Bone*, 110, 177–186. <https://doi.org/10.1016/j.bone.2018.01.035>

SUPPORTING INFORMATION

Additional supporting information can be found online in the Supporting Information section at the end of this article.

How to cite this article: Andrique, C., Bonnet, A. L., Dang, J., Lesieur, J., Krautzberger, A. M., Baroukh, B., Torrens, C., Sadoine, J., Schmitt, A., Rochefort, G. Y., Bardet, C., Six, I., Houillier, P., Tharaux, P. L., Schrewe, H., Gaucher, C., & Chaussain, C. (2024). Vasorin as an actor of bone turnover? *Journal of Cellular Physiology*, 1–22. <https://doi.org/10.1002/jcp.31257>